Lawrence Berkeley National Laboratory
Recent Work

Title
NUCLEUS-NUCLEUS TOTAL CROSS SECTIONS FOR LIGHT NUCLEI AT 1.55 AND 2.89 GeV/c/NUCLEON

Permalink
https://escholarship.org/uc/item/2t44b0jw

Author
Jaros, J.

Publication Date
1977-02-01

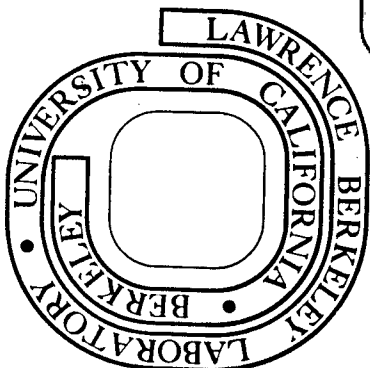# NUCLEUS-NUCLEUS TOTAL CROSS SECTIONS FOR LIGHT NUCLEI AT 1.55 AND 2.89 GeV/c/NUCLEON

J. Jaros, A. Wagner, L. Anderson, O. Chamberlain,
R. Z. Fuzesy, J. Gallup, W. Gorn, L. Schroeder,
S. Shannon, G. Shapiro, and H. Steiner

February 1977

DISCLAIMER

Nucleus-Nucleus Total Cross Sections for Light
Nuclei at 1.55 and 2.89 GeV/c/nucleon

J. Jaros, A. Wagner, L. Anderson, O. Chamberlain, R. Z. Fuzesy,

J. Gallup, W. Gorn, L. Schroeder, S. Shannon, G. Shapiro, and H. Steiner

February 1977

Nucleus-Nucleus Total Cross Sections for Light Nuclei at 1.55 and 2.89 GeV/c/nucleon[a]

J. Jaros,[b] A. Wagner,[c] L. Anderson, O. Chamberlain, R. Z. Fuzesy,
J. Gallup, W. Gorn,[d] L. Schroeder, S. Shannon, G. Shapiro, and H. Steiner

Lawrence Berkeley Laboratory and Department of Physics,

University of California, Berkeley, CA 94720

ABSTRACT

We have measured total cross sections for protons, deuterons, alphas, and ^{12}C on hydrogen, deuterium, helium, and carbon targets at 1.55 and 2.89 GeV/c/nucleon using the "good geometry" transmission method. In addition, we measured the inelastic cross sections and elastic slope parameters for reactions initiated by deuterons, alphas, and ^{12}C. Our results are in good agreement with Glauber theory predictions, but the factorization relation $\sigma_T(AA) = [\sigma_T(AB)]^2/\sigma_T(BB)$ is not a good guide. We find $\sigma_T \simeq 144(A_T^{1/3} - A_p^{1/3} - 1.48)^2$ mb and $\sigma_{IN} \simeq 78(A_T^{1/3} + A_p^{1/3} - 1.25)^2$ mb, where $A_T(A_p)$ is the atomic mass number of the target (projectile).

I. INTRODUCTION

We describe here an experiment performed at the Bevatron in which we measured the total cross sections for reactions initiated by protons, deuterons, alphas, and carbon nuclei on targets of hydrogen, deuterium, helium, and carbon. Measurements of proton-nucleus cross sections in the GeV/nucleon energy range have already been well explained in terms of Glauber's multiple scattering theory. [1,2,3] Using parameters describing nucleon-nucleon scattering and the known nuclear sizes, Glauber theory has accurately predicted these total cross sections without invoking any special effects. The formalism of the theory has been extended to encompass nucleus-nucleus collisions[4] and has been used by several authors[5,6,7,8,9] to predict total and inelastic cross sections for various nucleus-nucleus reactions.

The theory predicts that total cross sections are approximately proportional to the square of an interaction radius that goes as the sum of the radii of the colliding objects. If A and B are the atomic mass numbers of the target and projectile $\sigma_T(AB) \propto (A^{1/3} + B^{1/3})^2$. Deviations from this simple behavior might indicate the presence of new processes in these collisions. In view of the unique conditions that occur in collisions of nuclei, we may expect some surprises. A carbon-carbon collision at Bevatron energies can produce states of high energy density over a volume an order of magnitude greater than occurs in pp collisions. The Coulomb forces involved when large nuclei interact are no longer small compared to the nuclear forces. The interplay between the two should be important and interesting. The collision of two nuclei provides a new environment for nucleon-nucleon collisions. Does a proton which has interacted in one part of a nucleus behave as a "regular" proton in subsequent collisions?

An observation due to Gribov[10] also motivated this experiment. He noted that at very high energies Regge factorization leads to a very different A dependence for σ_T than that expected from geometrical grounds. The argument is as follows. The optical theorem relates $\sigma_T(AB)$ to the imaginary part of the elastic scattering amplitude F. If we assume this amplitude is dominated by the Pomeron, factorization lets us write it as $F \sim g_{PA}g_{PB}$, where g_{PA} is the coupling of a Pomeron to nucleus A at t = 0 and correspondingly for g_{PB}. Thus $\sigma_T(AB) \sim g_{PA}g_{PB}$, and similarly $\sigma_T(BB) \sim g_{PB}^2$ and $\sigma_T(AA) \sim g_{PA}^2$. Consequently, the "factorization relation" $\sigma_T(AA) = \sigma_T^2(AB)/\sigma_T(BB)$ obtains. If we use this to predict $\sigma_T(AA)$ from the input $\sigma_T(pA)$ and $\sigma_T(pp)$, and put $\sigma_T(pA) \sim A^{2/3}$, which roughly represents the data, we find $\sigma_T(AA) \sim A^{4/3}$. This differs radically from the behavior expected in a geometric picture where $\sigma_T(AA) \sim (A^{1/3} + A^{1/3})^2 \sim A^{2/3}$. Fig. 1 shows the differences between geometrical and factorization relation predictions for $\sigma_T(AA)$ as a function of A. The curve labelled "factorization" is based on measured values of $\sigma_T^2(pA)/\sigma_T(pp)$.

FACTORIZATION

GLAUBER THEORY

$\sigma_T(AA)$ (mb)

CC

$\alpha\alpha$

dd

A
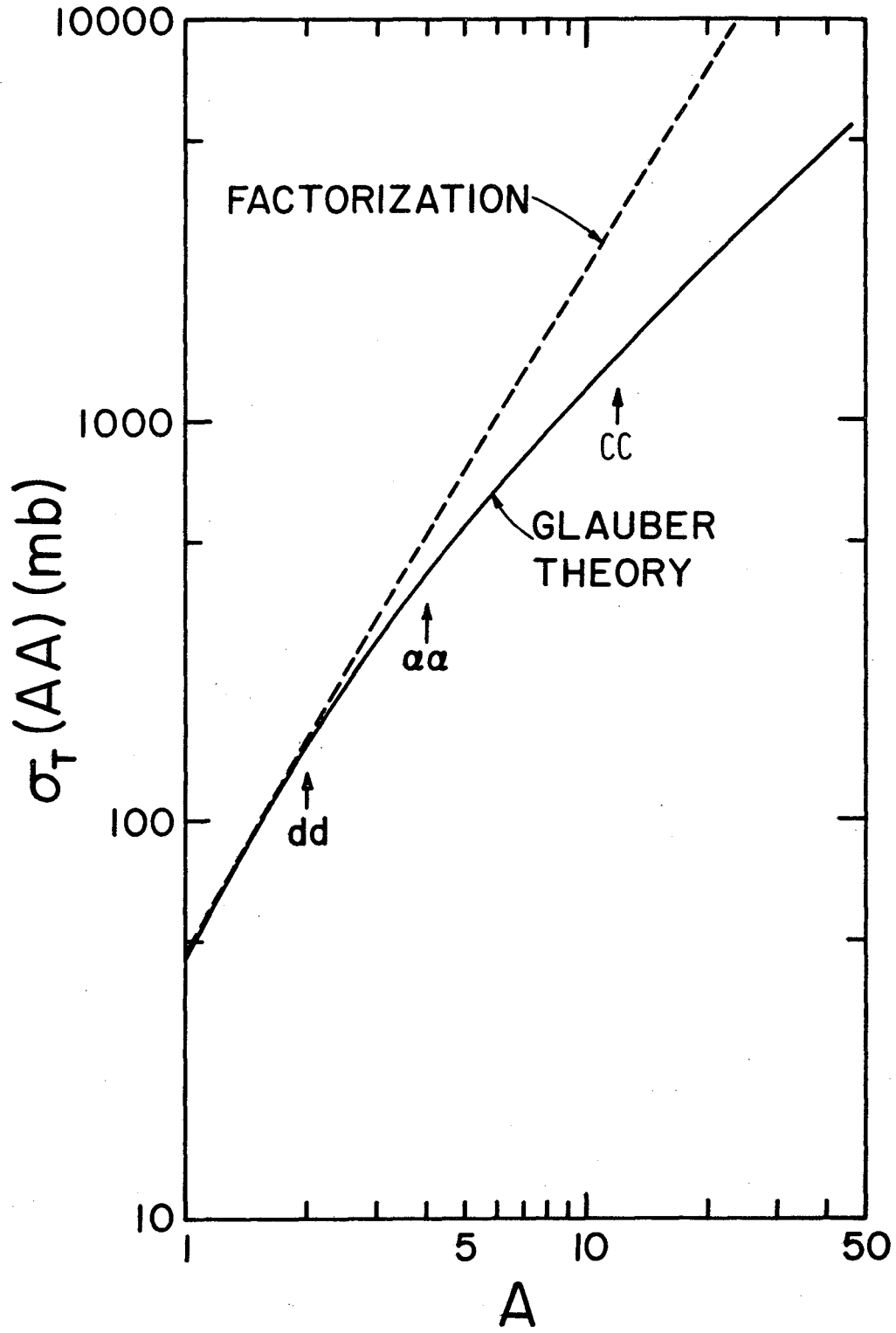
XBL 7511-9047

Fig. 1

II. Attenuation Measurements of Total Cross Sections

The art of measuring total hadronic cross sections with the so-called "good geometry" transmission technique has become quite refined in the past decade and a half. Several authors[11,12,13] discuss the technique as it is applied to multi-GeV pion, kaon, and proton interactions with various targets. Here we shall review the method and indicate the complications that crop up when it is applied to the study of nucleus-nucleus interactions.

A more detailed account of the experiment described in this paper can be found in the Ph.D. thesis of Jaros.[14]

The essence of the idea is very simple. (See Fig. 2.) A beam of particles, directed at the center of an array of coaxial disk counters, intercepts a target. If a beam particle interacts in the target, it and the other products of the interaction generally scatter out of the small solid angle the disk counters subtend. So, the smaller disks count the beam particles which have traversed the target without interacting. We call these transmitted beam particles "straight throughs." The total cross section, σ_T, is simply related to the number of particles transmitted, N_t, when N_B particles are incident

$$N_t = N_B \exp(-\eta \sigma_T)$$

Here η = (Number of target nuclei/unit area). Of course, it is possible that an interaction in the target produced a forward-going particle which is mistaken for a straight-through. The presence and magnitude of this effect can be inferred from the scattering into the larger disks by extrapolating the angular distribution at these wider angles to the forward direction.

In practice this is done by extrapolating the partial cross sections, σ_i. Let N_i be the number of particles disk i counts coincident with the passage

BEAM

TARGET

DISK COUNTERS
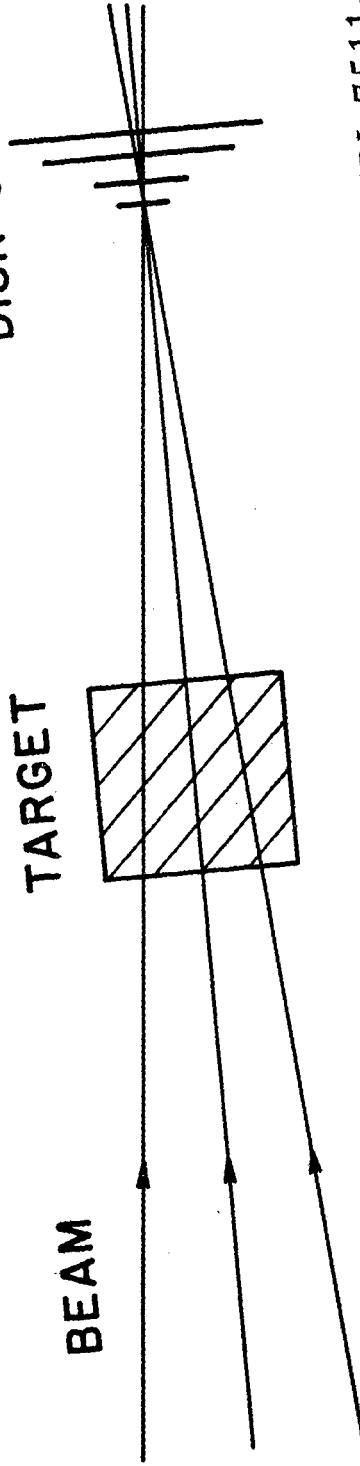
XBL 7511-9043

Fig. 2

of N_B beam particles. In the absence of empty-target effects the partial cross section is given by

$$N_i = N_B \exp(-n\sigma_i), \qquad \text{where}$$

σ_i is simply the cross section to scatter beyond disk i. In the limit that the solid angle subtended by disk i approaches zero, $\sigma_i \rightarrow \sigma_T$. To account for the inevitable presence of material in the beam other than the target, the set of measurements $\{N_i, N_B\}$ is repeated with the target removed. Call $D_i = N_i/N_B$ and designate with the superscript e (or f) target empty (or full) conditions. Then we have the practical relation

$$\sigma_i = \frac{1}{n} \ell n (D_i{}^e / D_i{}^f).$$

Each disk counter subtends a cone of half-angle θ_i from the target center; let t_i be the four momentum transfer squared corresponding to this angle, assuming elastic kinematics ($-t_i \sim p^2 \theta_i^2$, where p = incident particle's momentum). If we plot σ_i vs t_i (a "partial cross section plot"), the necessary extrapolation can be seen easily. (See Fig. 3.) The transmitted beam has some finite size at the disk counters due to finite spot size and multiple coulomb scattering in the target; hence much of the beam scatters out of the smallest angles, and the partial cross section there looks large. The bulk of the straight-throughs are caught at a larger $|t|$, along with some number of particles that did have nuclear interactions but scattered to small angles. The forward nuclear scattering, modified by coulombic effects, accounts for the appearance of the rest of the plot. The total nuclear cross section, i.e. the cross section we would measure in the absence of coulombic effects, can then be determined by extrapolating the partial cross sections from those regions where nuclear effects dominate to $t_i = 0$.

MULTIPLE COULOMB
SCATTERED STRAIGHT-THROUGHS

COULOMB-NUCLEAR
INTERFERENCE EFFECTS

NUCLEAR SCATTERING
DOMINATES

σ_T

LOG σ_i

$-t_i$
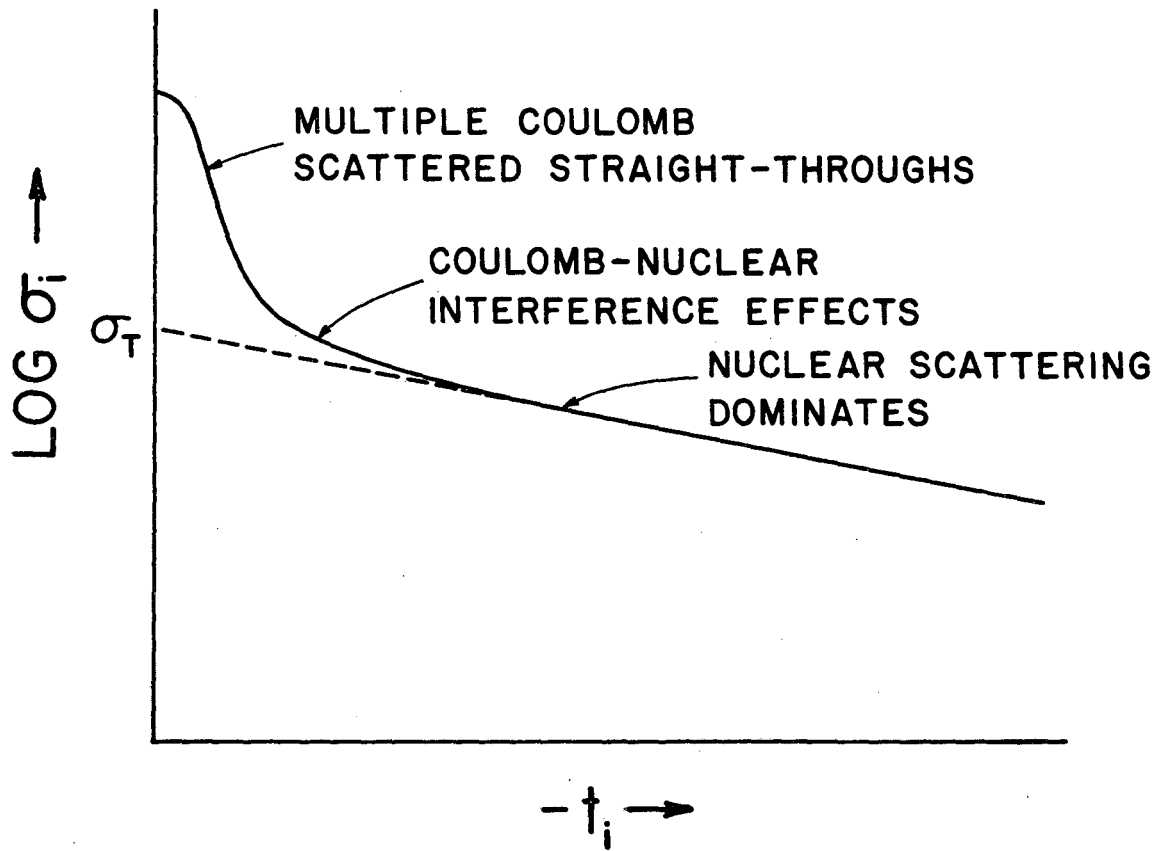
XBL 7511-9046

Fig. 3

Several features of nucleus-nucleus interactions complicate this procedure. The elastic scattering becomes more steeply forward peaked the larger the nuclei are. A simple diffraction picture leads us to expect the diffraction minimum to occur at an angle $\theta_{MIN} \propto \hbar/pd$, where p is the beam momentum and d is the size of the colliding objects. For nuclei of the same momentum per nucleon and nucleon number A, p ~ A and d $\propto A^{1/3}$; hence $\theta_{MIN} \propto A^{-4/3}$. Quantitatively we can consider the change in the slope parameter b of the differential elastic cross section, $d\sigma/dt \propto e^{bt}$. For pp scattering at 3 GeV/c, b = 6.5 $(GeV/c)^{-2}$. Simple optical models predict b = 200 $(GeV/c)^{-2}$ for CC scattering at the same momentum/nucleon. Such a steep diffraction pattern poses several experimental problems. The beam spot size clearly must be smaller than the nuclear diffraction pattern if the latter is to be cleanly resolved. This is difficult when the pattern is only 4 mr wide (as in the case of CC scattering at 3 GeV/c/nucleon). Beam stability is equally crucial. High angular resolution is required if the slope of the nuclear scattering is to be accurately determined. Finally multiple coulomb scattering must be minimized and thin targets used.

Coulomb effects become more important as the charges of the interacting nuclei increase. A convenient measure of their importance is the parameter $n = Z_1 Z_2 \alpha/\beta$, where Z_1 and Z_2 are the charges of the nuclei, α the fine structure constant, and β the relative velocity of the nuclei. The Rutherford cross section is proportional to Z^4 (for $Z = Z_1 = Z_2$). This means that coulomb-nuclear interference effects, which only mildly influence the differential scattering of protons on protons over the bulk of the elastic scattering, significantly alter the magnitude and shape of elastic CC scattering throughout the forward

diffraction peak. To extract purely nuclear parameters from such scattering requires that sizable corrections be made. The corrections themselves become uncertain because approximate methods must be used (perturbation theory becomes unwieldy for a coupling constant of order $6 \times 6 \times \alpha \sim 1/4$).

Nuclei have binding energies small compared to the projectile energies used in this experiment. Consequently, many channels are open beside elastic scattering, including projectile and target fragmentation, excitation, and particle production. As Greiner et al.[15] have shown, beam fragmentation processes have sizable cross sections and produce forward-going particles; such fragments can complicate the extrapolation procedure by adding extra terms to the angular dependence of the forward nuclear scattering. Preliminary measurements[16] indicate that excitation cross sections are appreciable and so must also be considered.

In view of these difficulties it is interesting to consider the limitations of the transmission technique for measuring nucleus-nucleus cross sections. To be specific, we shall use a simple black disk optical model for the scattering of a nucleus with radius R and charge Z by an identical nucleus. In this model the elastic cross-section is half the total cross-section, the forward amplitude can be taken to be purely imaginary, and the optical theorem then dictates the forward amplitude completely. We borrow the e^{bt} from particle physics and obtain the following relations.

$$\sigma_T = 8\pi R^2$$

$$\frac{d\sigma}{dt}_{NUC} = \frac{\sigma_T^2}{16\pi} \, exp \, \frac{t\sigma_T}{8\pi}$$

$$\frac{d\sigma}{dt}_{COUL} = \frac{4\pi n^2}{t^2} \, exp \, \frac{t\sigma_T}{8\pi} \, .$$

We have assumed the nuclear and electromagnetic form factors equal for simplicity.

The root-mean-square momentum transfer for multiple coulomb scattering is proportional to the thickness of the target and to the fourth power of Z. The average momentum transfer due to nuclear scattering goes as $1/\sigma_T$. In the limit of high Z, it would be necessary to use extremely thin targets with correspondingly small attenuations in order that multiple scattering does not hide more than a fixed fraction of the nuclear scattering.

There is another, more fundamental limitation to measuring total nuclear cross sections also imposed by the coulomb force. For sufficiently high Z, the Rutherford cross section will dominate the nuclear scattering for most of the elastic scattering, making the separation of coulomb and nuclear parts of the interaction dubious at best. Define t_{CN} such that $d\sigma/dt(t_{CN})_{COUL} = d\sigma/dt(t_{CN})_{NUC}$. Then $t_{CN} = 8\pi n/\sigma_T$. But $\langle t \rangle_{NUC} = 8\pi/\sigma_T$. Saying that the coulomb force dominates the scattering when $t_{CN} > \langle t \rangle_{NUC}$, we find that for n = 1 (i.e. Z ~ 12) the nuclear elastic scattering is lost in the coulomb signal.

The foregoing should warn us that total nuclear cross section is a concept useful in a limited domain of atomic number. It is our view that we can only get a good experimental determination of the nuclear total cross section if most of the elastic scattering occurs at angles where it is not dominated by the coulomb scattering. We feel the situation is manageable for Z = 6, but we would hesitate to try measurements for $Z \gtrsim 12$.

III. Experimental Set Up

To solve the measurement problems associated with heavy ions we have complemented the traditional disk counter array with multiwire proportional chambers (MWPC), an analyzing magnet, and dE/dx measurements. These additions provide increased angular resolution, isotope identification, and useful diagnostics. A general layout of the experimental set-up is shown schematically in Fig. 4.

A. The Beam

Beams of protons, deuterons, alphas, and carbon nuclei of 1.55 and 2.89 GeV/c/nucleon were obtained from the external beam of the Bevatron. The beam was designed to provide small, circular foci over a wide range of focal lengths and to be dispersionless at the final focus. It was tuned with the aid of MWPC's. Typical operating fluxes were 10 to 20 thousand particles/pulse with a pulse length about 1 second long. These low intensities were achieved by attenuating more intense beams from the source before injection into the main ring of the Bevatron. This guaranteed beam purity. The material in the beamline causes negligible beam contamination. In the worst case (^{12}C beams), we estimate that the beam is >99.5% $^{12}C_6$. The bulk of the contamination is due to interactions in one of the beam-defining counters, S2.

B. The Trigger Counters

To achieve the small and stable beam spot size this study of heavy ion reactions required, we used two MWPC's, P1 and P2, in the incident beam to select only those particles whose trajectories extrapolated to within 5 mm of the center of the array of disk counters. Chamber P2 had 1 mm wire spacing,
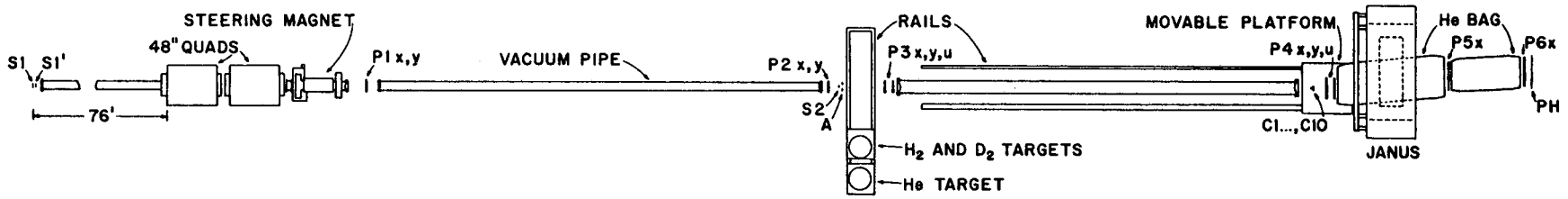
S1 S1'

48" QUADS

STEERING MAGNET

P1 x,y

VACUUM PIPE

P2 x,y

├── 76' ──┤

S2'
A

RAILS

P3 x,y,u

MOVABLE PLATFORM

P4 x,y,u

He BAG

P5x P6x

PH

C1...,C10

JANUS

H₂ AND D₂ TARGETS

He TARGET

XBL 7511-9306

Fig. 4

whereas all the other chambers had a wire spacing of 2 mm. The track selection was done with a matrix logic system. The details of the construction of the unit are given by Harms.[17]

Fig. 5 shows a comparison of the beam size with and without the matrix condition. With the matrix the spot size and the beam halo are significantly reduced, and the possibility of beam drift (a potential problem because the beam line is so long) is eliminated. The beam's position is defined by the position of P1 and P2 and the diode matrix; if the physical beam moves, we suffer a loss in the number of beam particles which satisfy the matrix trigger, but the position of the electronically selected beam remains unchanged. The fraction of actual beam particles satisfying the matrix condition varied from 20% to 4% depending on the focal length. The beam spot was $1.0 \pm .2$ cm FWHM at all focal positions.

Several scintillation counters were also used in the trigger. S1 and S1' were both situated at the intermediate focus F2. S2, placed just before the target, was made of 1.5 mm material to minimize beam contamination. The pulse height of S2 was recorded for a subset of the triggers to measure this contamination. Just following S2 was a large anticoincidence counter A, with a hole in its center slightly smaller than S2. Counter A was viewed by phototubes at each end and was designed to veto halo tracks coincident with a good track. We worried that it might also selectively veto legitimate target interactions which sent a charged particle backward, but we found no evidence for this effect.

The trigger requirement was a coincidence between S1, S1', S2, and the matrix output, with A in anticoincidence.
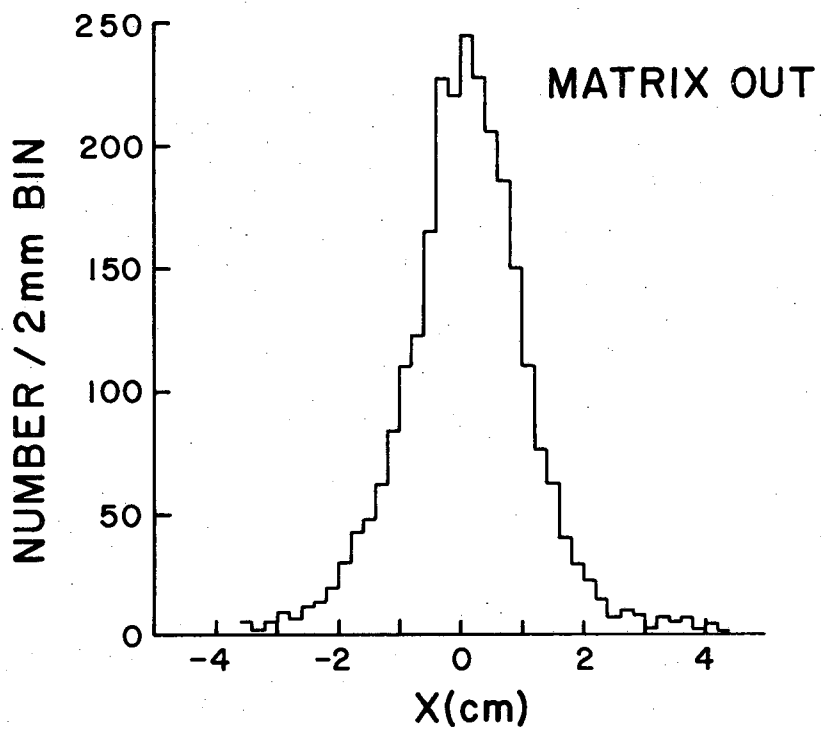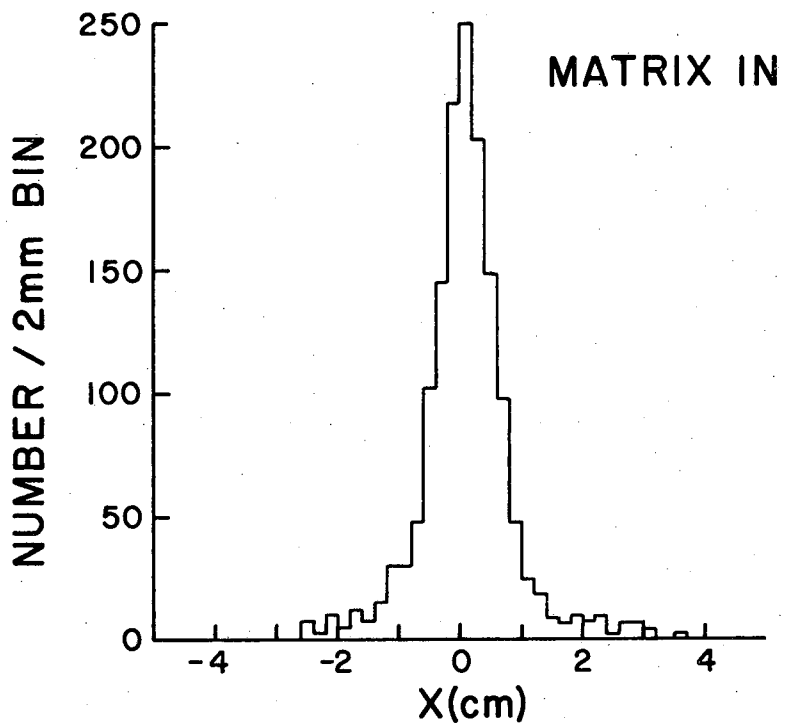
Fig. 5

XBL 7511-9048

C. Targets

Attenuation measurements were taken with hydrogen, deuterium, helium, and carbon targets. All the targets were positioned on a set of rails normal to the beam line and could be moved back and forth along the rails to center any particular target on the beam. This was done remotely with an accuracy of ±1.5 mm. A dummy target was included in the He target assembly. Target empty measurements for the liquid targets were made using this dummy target. We checked that these dummy runs agreed with runs made with the actual targets empty. The target-empty data for the carbon targets were taken by moving the entire target assembly so that no target intercepted the beam.

The flasks were mylar cylinders roughly 15 cm in diameter and 40 cm long, with 0.18 mm domed end caps. The flask lengths were chosen to obtain reasonably large attenuations ($\geq 10\%$) without causing excessive multiple coulomb scattering for p, d, and α projectiles. They were not optimally suited for carbon projectiles because the multiple coulomb scattering corrections are large in this case, but they were more than adequate to provide good cross checks with p,d, and α data from carbon targets. Each flask was fitted with a "bubble shield" which was simply a slightly smaller cylinder of mylar with open ends placed inside the flask. Its purpose was to deflect any bubbles which might arise from boiling at the bottom of the flask from the center region through which the beam passes. The flasks, which were insulated with aluminized mylar wrappings, were encased in two heat shields to minimize radiative heating. The inner one was held at LH (or LHe) temperature; the outer one was at LN temperature. The outer windows of the vacuum box were 0.5 mm mylar. The dummy flask was exactly like the others except that it was not wrapped with aluminized mylar or put into a low temperature heat shield. Instead, the extra insulating and window materials were hung at each end of the flask just inside the mylar

window of the outer vacuum jacket. The dummy flask was open to the surrounding vacuum.

The carbon targets were machined from graphite into blocks 15 cm square of thicknesses 0.635, 1.27, 2.54, and 5.08 cm.

The lengths of the flasks were measured under conditions which simulated the actual running conditions as much as possible. We put each flask into an aluminum box, evacuated the box, and filled the flask with liquid nitrogen. We determined the flask length by measuring the distance from each end of the box to the center of the flask's dome with a depth micrometer. By measuring a bar of known length with the same arrangement after we had removed the flask, we were able to deduce the flask's length accurately and reproducibly to ±.01 cm. We worried that the flask length might change after weeks of operations under vacuum but found, after long-term tests, that the effect was negligible (<0.05%/week). Measurements of one flask's length at the end of the run showed no appreciable change (<0.05%). The correction of the target lengths for the slight contraction of mylar as it is cooled from LN to LH or LHe temperatures is similarly small (<0.05%). Finally we made a plastic cast of the dome shape from one of the flasks so that we could measure the dome's contour accurately.

We used the target length and the target density to determine the number of target nuclei/unit area in each target. The density is, of course, a function of the temperature. The temperature was monitored during each run by two epoxy-coated carbon resistors situated near the top of each flask. These had been calibrated previously in liquid hydrogen, deuterium, and helium baths where the vapor pressure was known. Standard tables[18] were used to relate equilibrium vapor pressure to temperature and density. Given the average resistance for a series of runs with a given target, we thus knew the target density for those runs. We also monitored the vapor pressure directly during

the experiment as an independent measure of target density. The D and He densities determined by the two methods agreed to 0.1%, but the H density as determined from the resistors was 1.1% lower than that deduced from the vapor pressure. From the density and the target length, which was corrected for finite beam size effects using MWPC information and the measured curvature of the domes, we can deduce $\eta = N\rho\ell/A_T$, where $\rho\ell$ is the target thickness in gm cm^{-2}, A_T the atomic weight, and N is Avogadro's number. Table I gives the pertinent data on the various targets for a typical run. Target density was stable to better than 0.1% for any given running condition but varied as much as 1/2% during the course of the experiment. The finite beam size correction was largest for runs in the 10.8 m focal position (~0.5%) and was negligible for the 1.07 m focal position (~0.05%). The D target contained 2.2% H_2, but the data were easily corrected for this contamination.

Table I also summarizes the carbon target data. We used Union Carbide Grade ATJ graphite for the targets. The target dimensions were measured with micrometers. The target density was computed by weighing each of the targets and dividing by the target volume.

D. Disk Counter System

The disk counter system consisted of 10 coaxial circular disk scintillation counters mounted on a movable platform. We scaled the distance from the center of the target to the disk counters with the incident momentum. This arrangement allowed us to measure the angular distribution in the range $0 < -t < .030$ (GeV/c)^2 independent of the incident momentum. By using as many as 10 counters to cover this range in t, we achieved sufficient angular resolution to resolve even the sharp diffractive structure of CC elastic scattering.

TABLE I.

CHARACTERISTICS OF TARGETS.

Target	Number of Nuclei/mb	Target length(cm)
H_2	$1.7637 \pm .0026 \times 10^{-3}$	$42.093 \pm .01$
D_2	$2.0231 \pm .0038 \times 10^{-3}$	$40.098 \pm .01$
He	$8.1301 \pm .019 \times 10^{-3}$	$43.305 \pm .01$
C	$5.4019 \pm .005 \times 10^{-4}$	$0.635 \pm .003$
C	$1.0881 \pm .001 \times 10^{-4}$	$1.270 \pm .003$
C	$2.2125 \pm .002 \times 10^{-4}$	$2.540 \pm .003$
C	$4.3672 \pm .004 \times 10^{-4}$	$5.080 \pm .003$

The 10 disk counters, labelled $C_1,...C_{10}$, were fashioned from 1.5 mm thick scintillating plastic disks. We chose such thin material with the aim of reducing the number of interactions that would occur as particles traversed the disks en route to the isotope identification system. The light guides were also 1.5 mm plastic within 30 cm of the center of the counters and 3.0 mm beyond that. The sizes of the counters are given in Table II. The counters were arranged in order of increasing size with the smallest one upstream. The light guides were arranged to minimize the amount of material any particle would traverse before hitting a disk and to reduce the overlap of the light pipes of adjacent counters as much as possible. This last feature let us eliminate most counts coming from particles passing through a light pipe by requiring that every particle counted by disk i also be counted by disk i + 1. The counters used RCA 8575's which had been selected for low noise and high gain. The efficiency of counters 2 through 9 was monitored continuously during each run and was generally >99.99%. The efficiency of counters 2, 3, and 4 (which catch the bulk of the straight-throughs) was usually >99.999%.

The frame holding all 10 counters was mounted on a large stage which could be moved vertically or horizontally. This stage was secured to a steel platform which could be rolled on steel rails along the beam line between the target and the analyzing magnet JANUS. We chose five cart positions for data taking; the corresponding distances between the target center and counter C_2 were 1.07, 1.83, 3.66, 7.32, and 10.82 m. (The other disk counters were within 3 cm of C_2.) For all but the 1.07 m focal position we inserted an evacuated beam pipe between the target and the first disk counter to reduce the interactions of the beam in air. Such a precaution is essential in the case of C C interactions,

Table II. Disk counter dimensions.

Counter	Diameter (cm)
1	0.95
2	1.97
3	3.81
4	5.65
5	7.62
6	9.59
7	11.43
8	13.34
9	17.22
10	22.86

since 10 m of air is comparable to .63 cm C as a target. To be sure the beam was centered on the array of disk counters, we used a proportional chamber mounted just behind the disks, P4, to show the beam position and to show the position of C_1. By translating the counter array right-left or up-down, we could make these positions coincide and so center the beam on the disks to better than ± 1 mm.

E. Isotope Identification

The remaining components, MWPC's P3, P4, P5, and P6; the magnet JANUS; and a large scintillation counter whose pulse height was recorded, PH, were used to measure the angle of bend through JANUS, and the dE/dx of the exiting particle. Assuming that essentially all the beam fragmentation products have the original beam particle's velocity, bend angle and dE/dx information are sufficient to determine the charge and mass of the exiting isotope. Actually the fragments can have velocities slightly different from the beam, but the difference is small enough that isotope separation is still very clean. MWPC's P3 and P4 measure the particle trajectory before the bend, and P5 and P6 the trajectory after. P3 was located just downstream of the target and consisted of three separate planes, one measuring horizontal displacement (x), one vertical (y), and one at 45° (u). P4 was situated just behind the disks on the same movable cart and also had x, y, and u planes. P5 and P6 were both located after the bend, 1.81 m apart. Both chambers just had x planes, which suffice for measuring the angle of bend through the magnet. The bend angle resolution was generally limited by multiple scattering in the disk counters and gave $\Delta\theta/\theta = \Delta p/p \sim 4\%$. This was sufficient to resolve the various carbon isotopes.

JANUS is an H magnet with a gap 20 cm high, 56 cm along the beam direction, and 1.68 m wide that was positioned 38 cm to the left of the beam centerline.

The wide horizontal aperture allowed us to sample even relatively wide scattering angles in regions of uniform B field. We typically ran the magnet at 8 kG for 1.55 GeV/c/nucleon projectiles and 16 kG for 2.89 GeV/c/nucleon, giving $\int Bd\ell$ = 7.5 kGm or 15 kGm. Wire orbit studies showed that $\int Bd\ell$ was constant to better than 1% independent of entrance angle and entrance position for the particles we analyzed. This was sufficiently uniform that we could take the bend angle as directly proportional to the particle's rigidity.

The PH counter was a large rectangular scintillator 46 cm high by 63 cm wide and 1.25 cm thick, placed 18 cm behind P6 and viewed by phototubes from each side. It and the chambers P5 and P6 were positioned asymmetrically with respect to the beam line so that we could sample the widest possible range of scattering angles with a single geometry. The pulse height resolution was adequate for separating charge 5 from charge 6 and was uniform across the counter to better than 5%. As expected, the pulse height was proportional to the square of the charge with no sign of saturation up to Z = 6. To minimize the interactions of particles emerging from the disks we placed helium gas bags between the downstream end of P4 and the upstream side of P5 and between P5 and P6.

F. Electronics

Our measurement augmented the traditional total cross section technique with proportional chamber and pulse height information. The traditional method includes recording the number of incident particles and the number of counts seen by each of the disk counters coincident with an incident particle. This was done, but in addition, for a subset of the incident particles, we recorded all the wires "hit" in each of the proportional chambers, the pulse

height of S2 and PH, and a bit map of which disk counters fired. This full record was recorded for every tenth incident particle and for all particles scattering beyond the smallest two disk counters. Doing so let us sample the particles which hit each of the angular rings the disk counters define without being overwhelmed by the preponderance of straight-throughs that hit the first two rings.

Fig. 6 shows the trigger and disk counter electronics that is the heart of the experiment. We protected the circuitry from the passage of a second particle within the MWPC resolving time with a simple deadtime circuit. S2S was delayed with respect to S2L so that it would just fail to make coincidence with S2L's trailing edge. The passage of a second particle through S2 causes the output S2L to elongate and vetoes the trigger. The output of $\overline{SAM}$ signals the arrival of an incident particle that is aimed at the smallest disk. It is scaled, sent to gate the disk outputs, and fed to the event strobe. The disk counter electronics included a X 10 fast preamplifier, a fast discriminator, and a unit we called the "OR chain." Preamplifiers were needed to achieve very high efficiencies from the 1.5 mm plastic scintillators for minimum ionizing particles. The outputs of the preamplifiers were discriminated and sent to the OR chain. It OR's C_i with $C_{j<i}$ and gates the output C_i' with $\overline{SAM}$. This procedure minimizes the effect of ring-to-ring efficiency variations. All the outputs C_i' were scaled by Camac scalers and were recorded each Bevatron pulse. The event trigger (STROBE) was generated for every tenth $\overline{SAM}$ and whenever disks 1 and 2 were not hit (and so it was likely an interaction had occurred).

The MWPC readout electronics was developed by the Nuclear Instrumentation group at LBL and has been described in detail elsewhere.[19] Basically, one
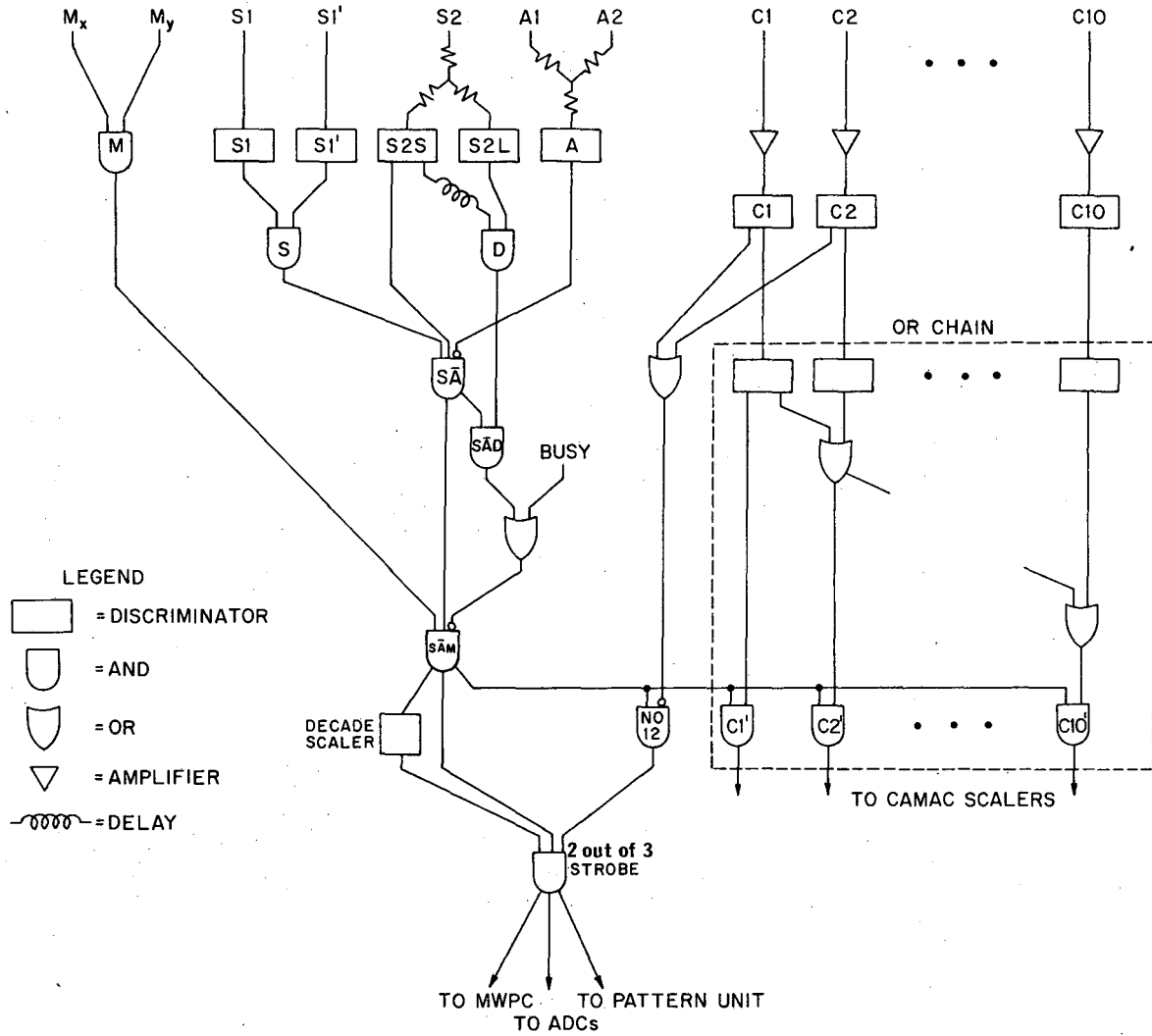
Fig. 6

XBL 7511-9351

or more hits on a plane generated a "fast out" pulse. It was discriminated and then gated by STROBE giving a "write gate." This signal was then sent back to the chambers where it enabled the event to be stored until it could be read out. By letting the fast out determine the write gate timing, we achieved 100% writing efficiency with a time resolution of 30 ns FWHM. This kept multiwire fires below 10% even when we ran the chambers at high enough voltages to guarantee high fast out efficiencies (>99%). A typical event had about 14 MWPC words in addition to 3 more words used to encode the other information (pulse height information from S2 and PH and trigger information).

A PDP-11/20 computer was used to store and monitor the incoming data. To handle high data taking rates (we could record up to 1000 events/pulse although we usually ran about 250 events/pulse), the incoming data were written into a circular buffer in the PDP-11 memory, which was continuously emptied onto disk. At the end of a pulse, all the scaler information was recorded and the information on disk transferred to magnetic tape. During this transfer a subset of the information was decoded to provide histogram displays for each MWPC plane and to monitor MWPC and disk counter efficiency.

G. Running Plan

We ran each of the target-full and target-empty conditions, usually re-peating each condition at least three times. There were typically 1000 SAM's and 200 STROBE's per pulse. A typical run lasted 30-45 minutes. We took sufficient data to give a statistical accuracy of about 0.3% to the raw partial cross sections. Run summaries were saved by the computer which allowed raw partial cross sections to be computed after we had finished a series of runs. This allowed us to make online rate studies and run-to-run consistency checks.

Table III summarizes our running conditions.

Table III. Running conditions.

PROJECTILE	KINETIC ENERGY/NUCLEON (GeV)	CART POSITION (m)	-t RANGE (GeV/C)^2
p	0.87	1.07	0 - .025
	2.1	1.83	0 - .031
d	0.87	1.83	0 - .035
	2.1	3.66	0 - .033
α	0.87	1.07	0 - .390
		3.66	0 - .038
	2.1	3.66	0 - .133
		7.32	0 - .032
C	0.87	3.66	0 - .342
		10.82	0 - .038
	2.1	7.32	0 - .290
		10.82	0 - .133

IV. Corrections to the Data

The essential data consisted of scaler records of the number of incident counts and the number of counts recorded coincidently in each disk i, called N_i. We use these scaler data to determine the angular distribution of transmitted and scattered particles in the forward direction. Of course inelastic processes (mostly projectile fragmentations) can contribute to these distributions. However, by using the MWPC and PH information to tag particles different from the projectile in charge, mass, or momentum, we can correct the distribution so it approximates that due to straight-throughs and elastic scatters alone. There are several advantages to this procedure: (1) We can eliminate contamination of the straight-throughs by beam fragments. (2) The angular distribution is not complicated by several terms with different t dependences, so the extraction of the cross-section is more reliable. (3) The data can be used to determine σ_E and the elastic slope parameter b in addition to σ_T. Aside from getting more information about the scattering, this detailed knowledge of the elastic differential cross section allows coulomb-nuclear interference corrections to be made with minimum dependence on specific models. This section will describe the correction of the data for such inelastic contaminants; in the next, we consider how to extract σ_T, σ_E, and b from these corrected distributions.

A. Corrections to ^{12}C Data

The data with ^{12}C incident were taken at the 10.82 m focal position for both the .87 and 2.1 GeV/nucleon runs. In this geometry, the isotope identification system samples events in all but the largest rings with nearly 100% efficiency. To accomodate the high specific ionization of a charge six particle without

saturating the disk counter electronics or swamping the MWPC's with delta rays, we lowered their respective high voltage supplies. This made the chambers insensitive to $Z < 4$ and the disks insensitive to $Z < 3$; however, both were fully efficient for $Z = 6$.

Using pulse height and trajectory information we corrected the raw scaler data for contamination in the beam and projectile fragmentation in the target. The corrected scaler readings were those we would have measured if the disk counters were sensitive only to ^{12}C with the momentum of the incident beam and if the beam were pure ^{12}C.

Beam contamination was effectively eliminated by requiring that counter S2 have a pulse height consistent with the passage of a charge 6 particle. We corrected the number of incident particles by multiplying it by the ratio of charge six particles to all incident particles. The corrected number is $(\overline{SAM})'$.

A bit map showing which disks were hit let us determine through which ring the particle passed. Let us consider the R_i particles which passed through ring i. A fraction g_i of these were due to right-momentum ^{12}C. We measure g_i by finding what fraction of the R_i particles have charge and rigidity consistent with being ^{12}C. Since the isotope identification system sampled particles after they had traversed the disk counters, where some fraction $(1 - f_i)$ interacted, the measured ratio of right-momentum ^{12}C to all particles is given by $f_i g_i$. We express this ratio as the product of two factors. The first is the fraction of particles that had a pulse height consistent with $Z = 6$, $f_{Z,i}$. This is just the fraction of events with non-zero pulse height found above the cut shown in Fig. 7. As the figure shows, there was a clear separation between $Z = 5$ and $Z = 6$; we subtract a small background corresponding to the tail of the $Z = 5$ distribution that extends above the cut. The second factor
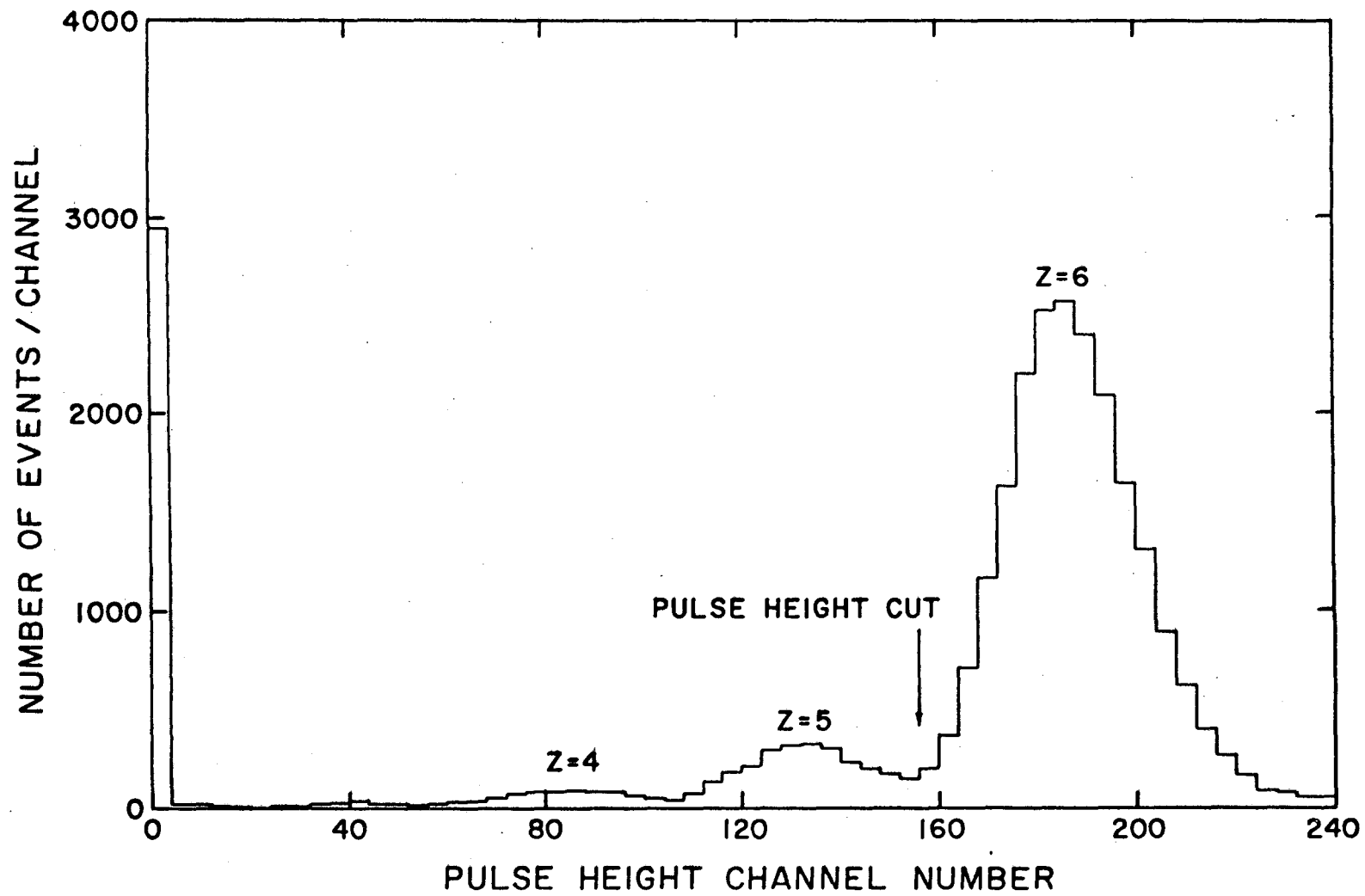
XBL 7511-9096

Fig. 7

is the fraction of particles with $Z = 6$ that had an angle of bend consistent with that expected for ^{12}C at the incident energy $f_{\theta,i}$. This is the fraction of events with a well-defined bend angle equal to that of the incident particle. Fig. 8 shows the clear separation of the ^{11}C and ^{12}C isotopes and the cuts appropriate for the definition of ^{12}C. The width of the ^{12}C peak was consistent with that due to multiple coulomb scattering in the disk counters and the known chamber resolution. We saw no evidence of ^{12}C production at momenta below the incident beam momentum.

It remains to determine the fractions f_i, the transmission probability for ^{12}C on ring i. Essentially all particles hitting the smallest disk were right-momentum ^{12}C; this is borne out by the observation that $f_{Z,1} f_{\theta,1}$ (target full) $= f_{Z,1} \; f_{\theta,1}$ (target empty). Thus $g_1 = 1$ and f_1 is given by

$$f_1 = \frac{1}{g_1} f_{Z,1} \times f_{\theta,1}.$$

$(1 - f_1)$ is the probability that a right momentum ^{12}C which hit ring 1 did interact in passing through the disks or the subsequent material. Let r be the fraction of all these interactions that occurred in the disks. We calculate r using optical model predictions for σ_{IN}. Since all the disks had the same thickness, the probability of interaction in any disk was $(1 - f_1)r/10$. The number of disks a particle hitting ring i had to pass through was $(11 - i)$; hence a particle hitting ring i had a probability of interacting in the disks given by $(11 - i)(1 - f_1)r/10$. It had an additional probability $(1 - f_1)(1 - r)$ of interacting in the subsequent material. So

$$(1 - f_i) = (11 - i)(1 - f_1)r/10 + (1 - f_1)(1 - r)$$

or

$$f_i = f_1 + \frac{i - 1}{10} r(1 - f_1).$$
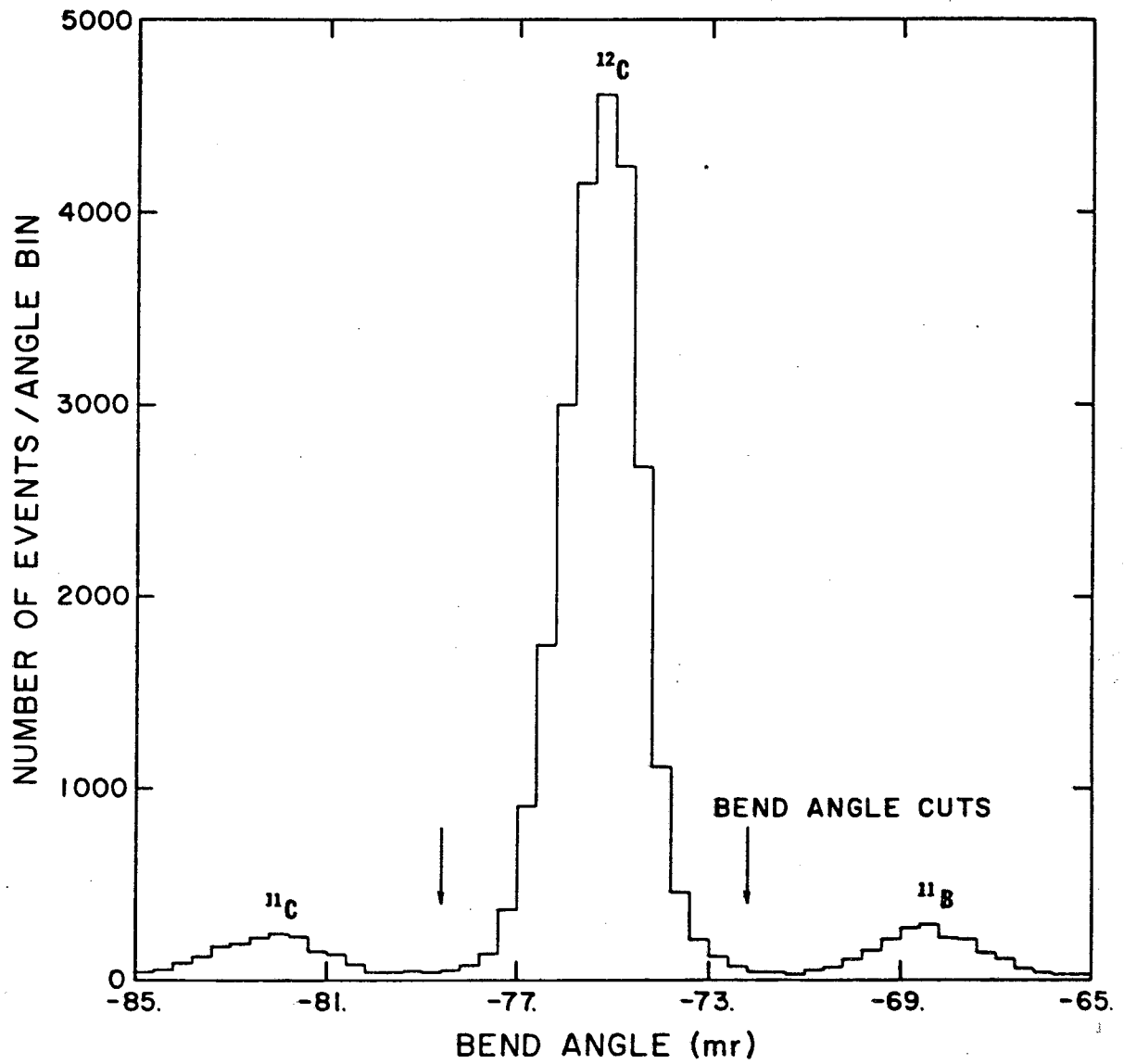
XBL 7511-9094

Fig. 8

The derived partial cross sections are quite insensitive to the choice of r; varying r (which is typically .80) between .40 and 1.0 causes σ_T to vary negligibly and σ_E to vary by 2%.

Given the f_i and R_i, the raw counts seen by each ring as determined by the scalers, we compute the corrected ring counts, normalized by the number of incident particles:

$$R'_i = \frac{R_i}{SAM}, \times f_{z,i} \times f_{\theta,i} \times \frac{1}{f_i}.$$

Then the corrected disk counts are:

$$D'_i = \sum_{j \le i} R'_j.$$

From D'^e_i and D'^f_i we compute the corrected partial cross sections as usual:

$$\sigma'_i = \frac{1}{n} \ln(D'^e_i / D'^f_i).$$

B. Corrections to the Deuteron and Alpha Data

The data with alphas incident were taken at the 3.66 and 7.32 m cart positions, the data with deuterons at the 1.83 and 3.66 m positions for the 0.87 and 2.1 GeV/nucleon running, respectively. In these cart positions the isotope identification system no longer sampled particles which hit the rings with full geometric acceptance. This fact required us to revise the approach used in the analysis of the ^{12}C initiated reactions.

As in the ^{12}C analysis, we measure the fraction g_i of all the events hitting ring i that are due to alphas (or deuterons) with the rigidity of the beam. Again, the presence of material in the isotope identification system causes interactions, so our measurement of this fraction gives $f_i g_i$. But now, since the isotope identification system has less than full acceptance, we can measure

$f_i g_i$ only for the subset of the particles in a ring which have a trajectory, as determined by P3 and P4, that extrapolates through the rest of the system. We extrapolate the trajectory, assuming the particle has the rigidity of the beam. For this running, both the disks and the MWPC's were fully efficient for minimum ionizing particles, so all events were sampled uniformly. In the case of .87 GeV/nucleon deuterons, we sampled too little of the elastic scattering region to extract σ_{IN} or σ_E reliably.

We express $f_i g_i$ as a product of three factors. The first is the fraction $f_{\theta,i}$ of particles that have an angle of bend consistent with that expected for the incident particles. The second is a factor that corrects for slight inefficiencies in chambers 5 and 6, $1/\epsilon_{56}$ ($\epsilon_{56} \simeq .96$). The third is the fraction $f_{Z,i}$ of those particles which have satisfied the bend angle criterion and that have a pulse height consistent with that expected for the incident particles. (Since the bend angle cut alone can separate deuterons from their proton fragments, we set $f_{Z,i} \equiv 1$ for the deuteron initiated reactions). Beam contamination effects were negligible. As shown in Figs. 9a, 9b, and 10, beam fragmentations were easily identified.

We find the interaction ratios f_i just as we did with ^{12}C. Then given f_i and R_i, the raw scaler counts for ring i, we compute the corrected ring counts normalized by $\overline{SAMS}$ as

$$R'_i = \frac{R_i}{\overline{SAM}} \times f_{\theta,i} \times f_{Z,i} \times \frac{1}{\epsilon_{56}} \times \frac{1}{f_i} .$$

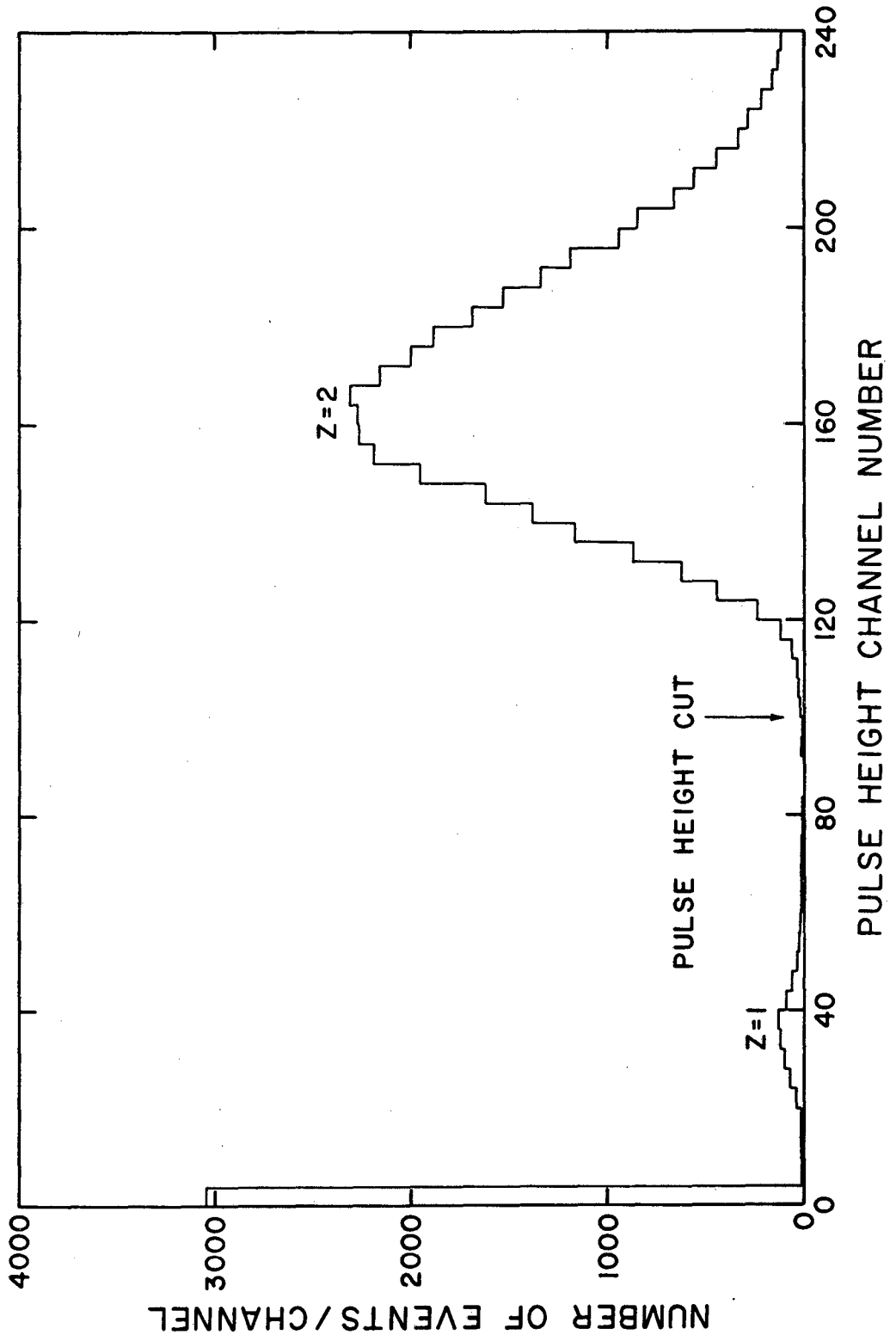From this we compute the corrected disk counts and the corrected partial cross section as before.

C. Corrections to the Proton Data

The proton data were taken at the 1.07 and 1.83 m cart positions for the .87
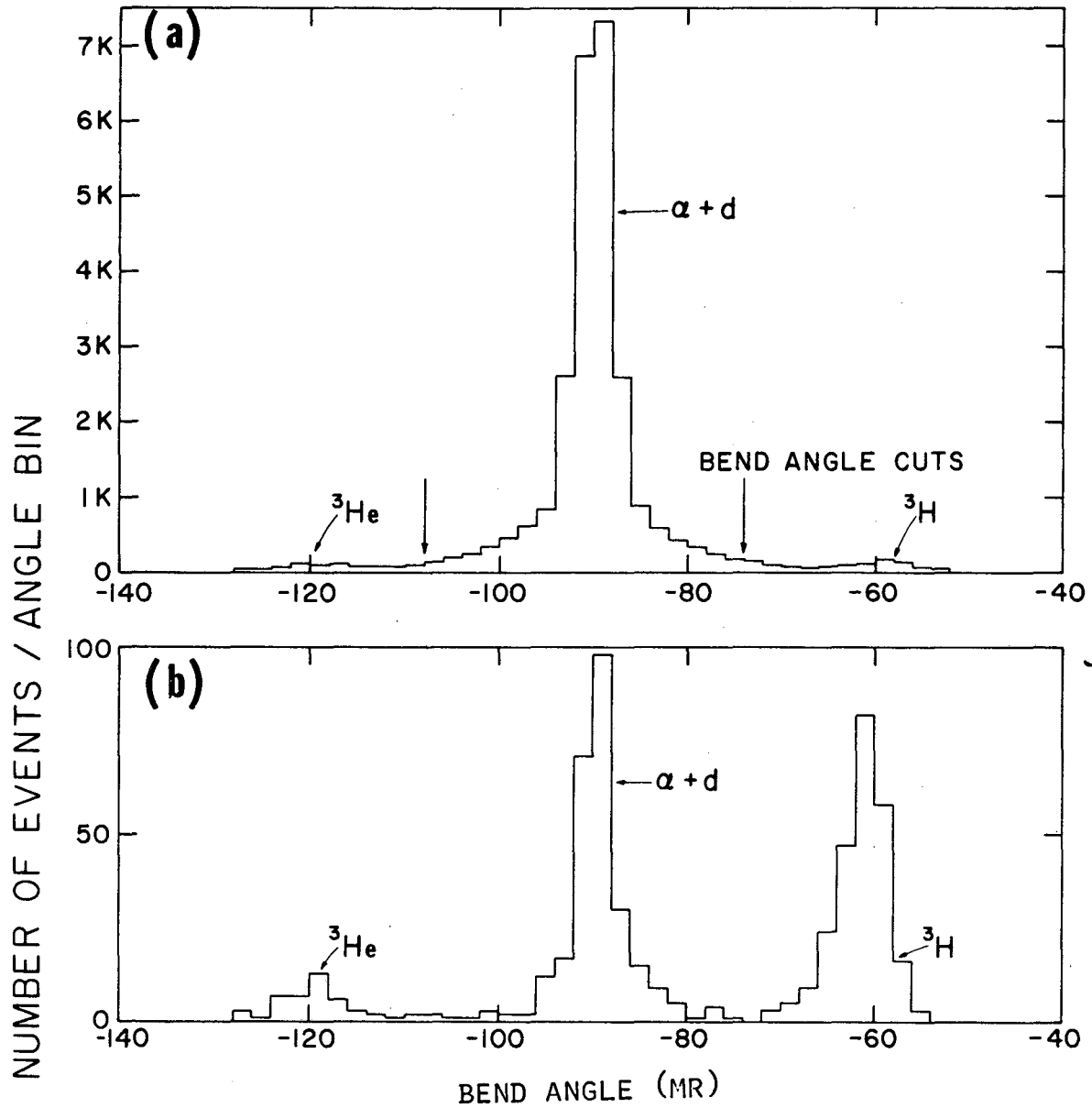
XBL 7511-9093A

Fig. 9

Fig. 10

XBL 7511-9095

and 2.1 GeV running, respectively. In these geometries the magnetic analysis system subtends such a small solid angle that only a small part of the angular distribution could be corrected. Consequently we abandoned the correction scheme in this case and relied on the traditional extrapolation techniques.

V. Data Analysis

In this section we elaborate the method used to extract the total nuclear cross section from the corrected partial cross sections.

Traditionally this is done by first correcting the measured partial cross-sections for coulomb and other effects (such as finite beam size and divergence or multiple scattering) and then extrapolating these corrected cross-sections to zero solid angle. This approach assumes that one can isolate two components of the observed angular distribution, the straight-throughs and the elastic scatters. When the average angle in multiple coulomb scattering is very much less than the average angle of nuclear scattering, this is a good approximation. One can then correct for the multiple coulomb scattering of the straight-throughs, and for the single coulomb scattering and the coulomb-nuclear interference of the elastic scatters.

But when the average momentum transfers in the two cases are comparable, as they are for several of the reactions we have studied (because the elastic scattering is so forward peaked), the approximation fails. It fails because the coulomb scattering, unlike its nuclear counterpart, can't be divided into straight-throughs and elastic scatters. Every particle coulomb scatters.

There is another problem to be faced here. The corrections for multiple scattering and coulomb-nuclear interference depend on the parameters describing the elastic scattering and the total cross-section. Since these have not yet been measured, the corrections are model dependent.

We manage the coulomb corrections by extending a suggestion made to us by Alfred Goldhaber that allows multiple coulomb scattering effects to be included exactly. We minimize dependence on models by fitting the observed

angular distributions to obtain parameters that describe the elastic scattering. Not only does this allow us to make the corrections more accurately, but it yields extra information from the measurements.

Our approach goes roughly as follows. We calculate the angular distribution seen by the disk counters, by assuming values for σ_T and the elastic scattering parameters and using the known target length, beam divergence, and geometry. Integrating this distribution over the angles subtended by the disks for both target full and target empty conditions gives the ratios R_i, from which we compute the partial cross-sections. These we compare to the data, and with standard fitting procedures we vary the input parameters until we have good agreement.

Let us distinguish here between a differential scattering law, $d\sigma/dt$, and the angular distribution, $f(\theta,\ell)$ that results when particles scatter according to that law through a target of thickness ℓ. These distributions differ from their associated differential laws because not all the beam interacts (so there are straight-throughs) or there are multiple interactions. For example, the Moliere distribution,

$$f_M(\theta,\ell) \sim \exp\left[-\theta^2/\theta_0^2(\ell)\right],$$

results from Rutherford scattering according to the law,

$$d\sigma/dt \sim t^{-2}.$$

We will denote the connection between a scattering law and its resultant distribution with an arrow:

$$d\sigma/dt \rightarrow f(\theta,\ell).$$

We normalize $f(\sigma, \ell)$ such that

$$N(\theta_0) = \int_0^{\theta_0} \theta \, f(\theta, \ell) d\theta$$

where $N(\theta_0)$ = the fraction of incident particles scattered by angles less than or equal to θ_0. The following important theorem can be proved:[14]

If $\qquad d\sigma/dt = (d\sigma/dt)_1 + (d\sigma/dt)_2$

and $\qquad (d\sigma/dt)_i \rightarrow f_i(\theta) \qquad\qquad$ for $i = 1, 2,$

then $\qquad d\sigma/dt \rightarrow f(\theta),$

where $\qquad f(\theta) = \dfrac{1}{2\pi} \int_0^{2\pi} d\phi' \int_0^{\infty} \theta' d\theta' f_1(\theta') f_2(\theta'')$

and $\qquad \theta'' = (\theta^2 - \theta'^2 - 2\theta\theta'\cos\phi')^{1/2}.$

The integral is just the two-dimensional fold of the distributions f_1 and f_2. This result is exact in the limit that the scattering is forward, a very good approximation in all the reactions we have measured.

To use the theorem we write

$$\frac{d\sigma}{dt} = \frac{d\sigma}{dt}_{\text{POINT COULOMB}} + \frac{d\sigma}{dt}_{\text{REMAINDER}}.$$

Here $d\sigma/dt$ is the elastic differential cross section for a nucleus-nucleus interaction and includes all nuclear and coulomb effects.

Molière has done the hard part of the problem by finding the multiple coulomb scattering distribution

$$\frac{d\sigma}{dt}_{\text{POINT COULOMB}} \rightarrow f_M(\theta, \ell).$$

Let us define the "remainder" distribution $f_R(\theta, \ell)$ by the statement

$$\frac{d\sigma}{dt}_{\text{REMAINDER}} \rightarrow f_R(\theta,\ell).$$

We can determine the actual scattering distribution, $f(\theta,\ell)$, by first determining the remainder distribution, $f_R(\theta,\ell)$, and folding it with the Molière distribution $f_M(\theta,\ell)$.

The Molière distribution can be given[20] in terms of a series expansion in a parameter, γ^{-1} ($\gamma \sim 10$ for our conditions):

$$f_M(\theta,\ell)\, \theta d\theta = \nu d\nu\, [2 \exp(-\nu^2) + \gamma^{-1}f_1(\nu) + \nu^{-2}f_2(\nu) + \ldots]$$

where

$$\nu = (\theta/\theta_c)\gamma^{1/2}$$

and γ is given by

$$\gamma - \ln\gamma = 2\, \ln(\theta_c/\theta_a) - 0.154$$

$$\theta_a = 4.49 \times 10^{-3}\, Z_T^{1/3}(1 + 3.35n^2)^{1/2}/p$$

$$\theta_c = 0.396\left[Z_T(A_T + 1)/A_T\right]^{1/2} Z_p\, \ell^{1/2}/\beta p$$

$$n = Z_p Z_T\, \alpha/\beta.$$

Z_T, A_T, and Z_p are the target nucleus charge, mass number, and the projectile charge. p is the projectile momentum, in MeV/c; ℓ the target thickness, in gm/cm^2; β the projectile velocity; and α the fine-structure constant. Bethe[21] has tabulated the functions f_1 and f_2. We note that the average angle in multiple coulomb scattering is $\theta_c\gamma^{1/2}$.

In practice we compute the distribution by evaluating θ_a and θ_c, finding γ iteratively, and approximating $f_M(\theta,\ell)$ with the first three terms of the

expansion out to an angle ten times the mean multiple coulomb scattering angle. Beyond this point we truncate $f_M(\theta,\ell)$ to zero. Since the functions $f_1(\nu)$ and $f_2(\nu)$ are given only for discrete values of ν, we tabulate $f_M(\theta,\ell)$ only for the corresponding values. For intermediate angles we use a Gaussian interpolation.

For a given $d\sigma/dt$, we can compute $d\sigma/dt_R$ and then approximate the remainder distribution $f_R(\theta,\ell)$. We parameterize the nuclear scattering with σ_T, δ(the ratio of real to imaginary part of the nuclear scattering amplitude), and b (the nuclear slope parameter). Let e^{Bt} and e^{Ct} be the electromagnetic form factors for the projectile and target nuclei. We can write the elastic scattering as the sum of nuclear, coulomb and coulomb-nuclear interference terms according to approximations derived by Bethe.[22]

$$\frac{d\sigma}{dt} = \frac{(1 + \delta^2)}{16\pi} \sigma_T^2 e^{bt} \mp \frac{4\pi\eta^2}{t^2} e^{2(B+C)t} - \frac{\eta\sigma_T}{|t|} e^{(b/2+B+C)t}(\delta\cos\eta\phi + \sin\eta\phi)$$

where

$$\phi = -\ln(1.78\ Dt)$$

and

$$D = b/2 + B + C.$$

Note that we have used the optical theorem to express the magnitude of the elastic scattering in terms of σ_T and δ. We have assumed that elastic scattering dominates the distributions we have measured and that the nucleus-nucleus elastic differential cross section can be adequately parameterized with a simple exponential. We assume further that that δ does not change with t, at least over the t-range covered in this experiment.

These assumptions are justified, *a posteriori*, by the facts that the above parameterization can represent the data very accurately and that the values of

σ_E and b derived from the fits agree with previous measurements of those quantities, where those measurements exist (for example, proton-carbon reactions). Franco[23] has shown that the approximation Bethe used in deriving $d\sigma/dt$ becomes less accurate as the charges of the target and projectile increase. However, he finds that the corrections to $d\sigma/dt$ are at most of order 10% even in our most severe case (carbon-carbon scattering with $|t|$ less than .01 $(GeV/c)^2$). Such corrections would modify σ_T by less than one percent, and so will be ignored.

We have in some cases chosen a slightly different parameterization. We add σ_E as an input parameter and no longer impose the optical theorem. This amounts to replacing σ_T, in Bethe's formula for $d\sigma/dt$, by

$$g^2 = 16\pi \, \sigma_E \, b/(1 + \delta^2).$$

The optical theorem makes b very sensitive to small changes in σ_E and δ in those reactions (initiated by deuterons and alphas) whose forward diffraction peaks do not wholly lie within the range of the disk counters. In these cases small errors in σ_T (say, ten percent), and our uncertainty in δ, can lead to 100% errors in b. This situation is ameliorated if we use the alternate parameterization. The values we derive for σ_T, σ_E, and b are consistent with the optical theorem.

We treat σ_T, σ_E, and b as variables in the expressions above, and δ, B, and C as known constants. B and C are measured in electron scattering experiments.[24] Unfortunately we have no real knowledge of δ and are forced to rely on model calculations which relate δ(nucleus-nucleus) to δ(proton-proton). The latter has been measured by observing the coulomb-nuclear interference. Although coulomb-nuclear interference effects are significant in our data, we have not

attempted to measure δ by including it as one of the parameters of our fit. The interference dip appears around $-t = .001$ $(GeV/c)^2$ and, in this experiment, is lost in the multiple coulomb scattering. This leaves only the region at larger $|t|$ where the interference effects are subtle and hard to untangle unambiguously.

We have chosen to use formulas given by Fishbane and Trefil[7] to evaluate δ. They derive a simple expression for the elastic scattering amplitude in the "optical limit" of Glauber theory in terms of the nucleon-nucleon parameters and the radii of the colliding nuclei. Table IV summarizes the values of B or C and δ used in evaluating $d\sigma/dt$.

Figures 11a, b, and c show model calculations of the elastic scattering for the reactions pp, pC, and CC. Note how the Coulomb scattering becomes a more and more significant feature as the target and projectile charges increase. Figure 12 shows schematically the behavior of $(d\sigma/dt)_R$. Since the interference term may be negative near t_{CN} and it dominates $(d\sigma/dt)_R$ as $t \to 0$, $(d\sigma/dt)_R$ goes negative in the region $-.0003 > t > -.001$ $(GeV/c)^2$ for some reactions, such as carbon-carbon. This rapidly oscillating behavior poses computational problems when we fold $f_R(\theta)$ with $f_M(\theta)$. To circumvent this pathological behavior, we define $(d\sigma/dt)_R'$ to equal $(d\sigma/dt)_R$ and to be a smooth continuation of it where the problems start. In some cases $(d\sigma/dt)_R'$ differs from $(d\sigma/dt)_R$ only at angles well within the typical multiple scattering angle. At worst these angles are comparable. We can show [reference 14, p. 75ff.] that the small t behavior of $(d\sigma/dt)_R'$ does not affect the results.

We can now derive $f_R(\theta,\ell)$ from $(d\sigma/dt)_R'$, by re-introducing Coulomb effects. We do this in two steps. First we turn on all electrical effects except the singular direct point Coulomb part of the cross section, $(d\sigma/dt)_{PC} = 4\pi n^2/t^2$. Only later, with the help of Molière, will the point Coulomb effects be included.

Table IV. Form factors and Re/Im ratios.

Particle	B $(GeV/c)^{-2}$
p	2.74
d	16.
α	11.
C	25.

Reaction	δ (.87 GeV/nuc)	δ (2.1 GeV/nuc)
pp	.080	-.29
pd	.075	-.27
pα	.067	-.24
pC	.061	-.22
dd	.074	-.27
dα	.068	-.24
dC	.057	-.20
αα	.053	-.19
αC	.041	-.14
CC	.030	-.10

2.1 GeV pp

COULOMB SCATTERING

NUCLEAR SCATTERING

COULOMB-NUCLEAR INTERFERENCE

$d\sigma/dt \ (b/(GeV/c)^2)$

$-t \ ((GeV/c)^2)$

XBL 7511-9049

Fig. 11a

Fig. 11b

XBL 7511-9050

2.1 GeV/NUC CC

COULOMB SCATTERING

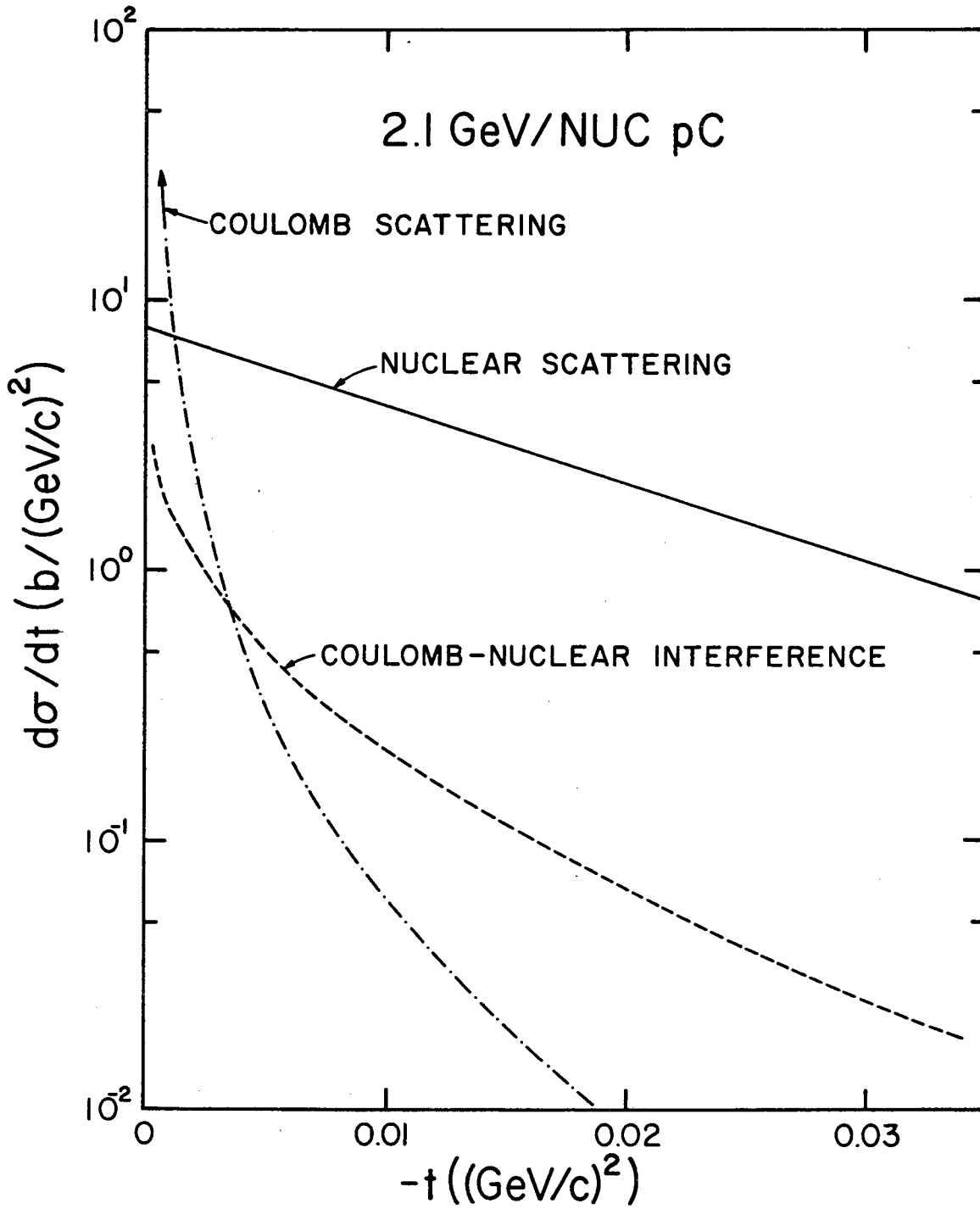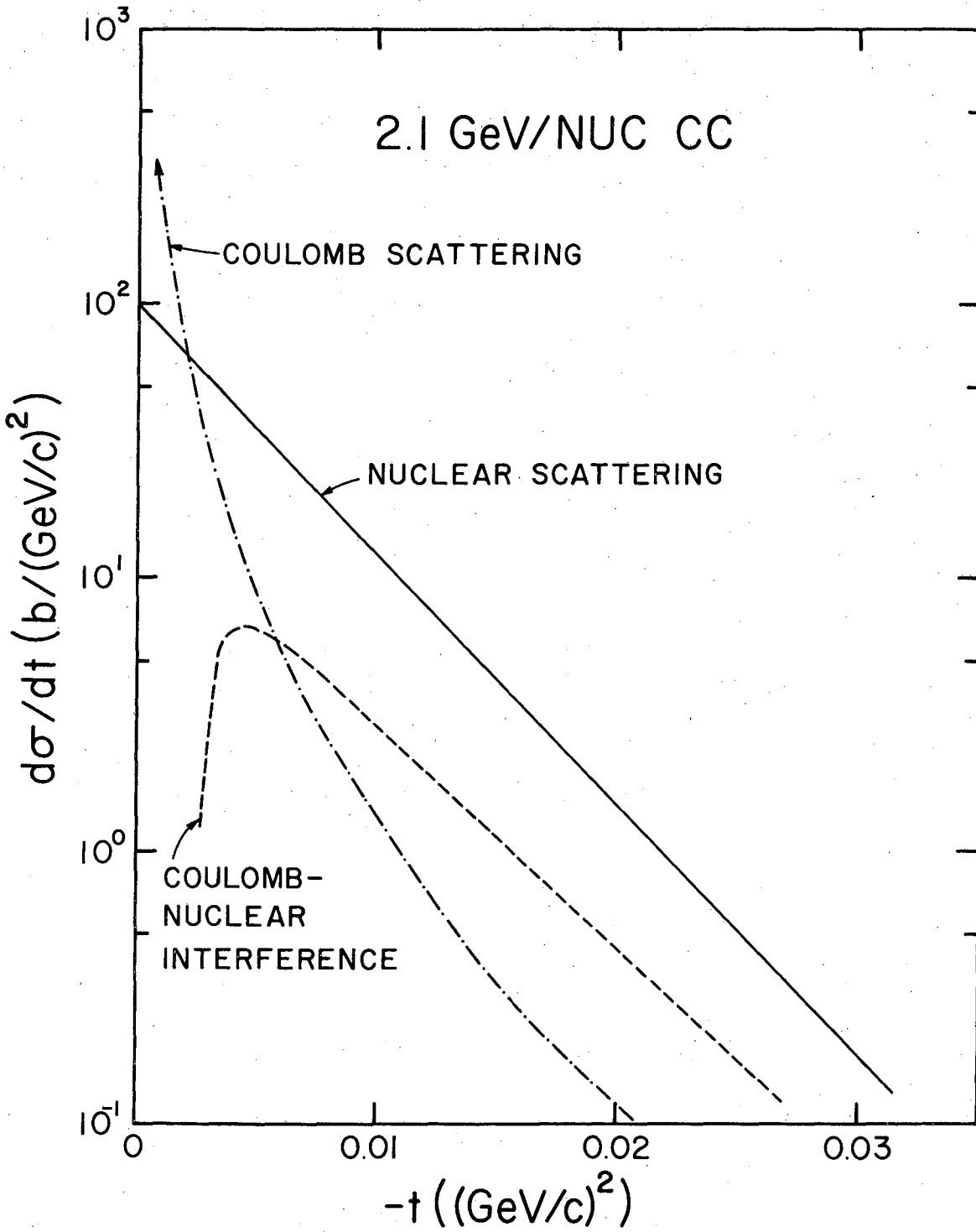NUCLEAR SCATTERING

COULOMB-NUCLEAR INTERFERENCE

$d\sigma/dt\ (b/(GeV/c)^2)$

$-t\ ((GeV/c)^2)$
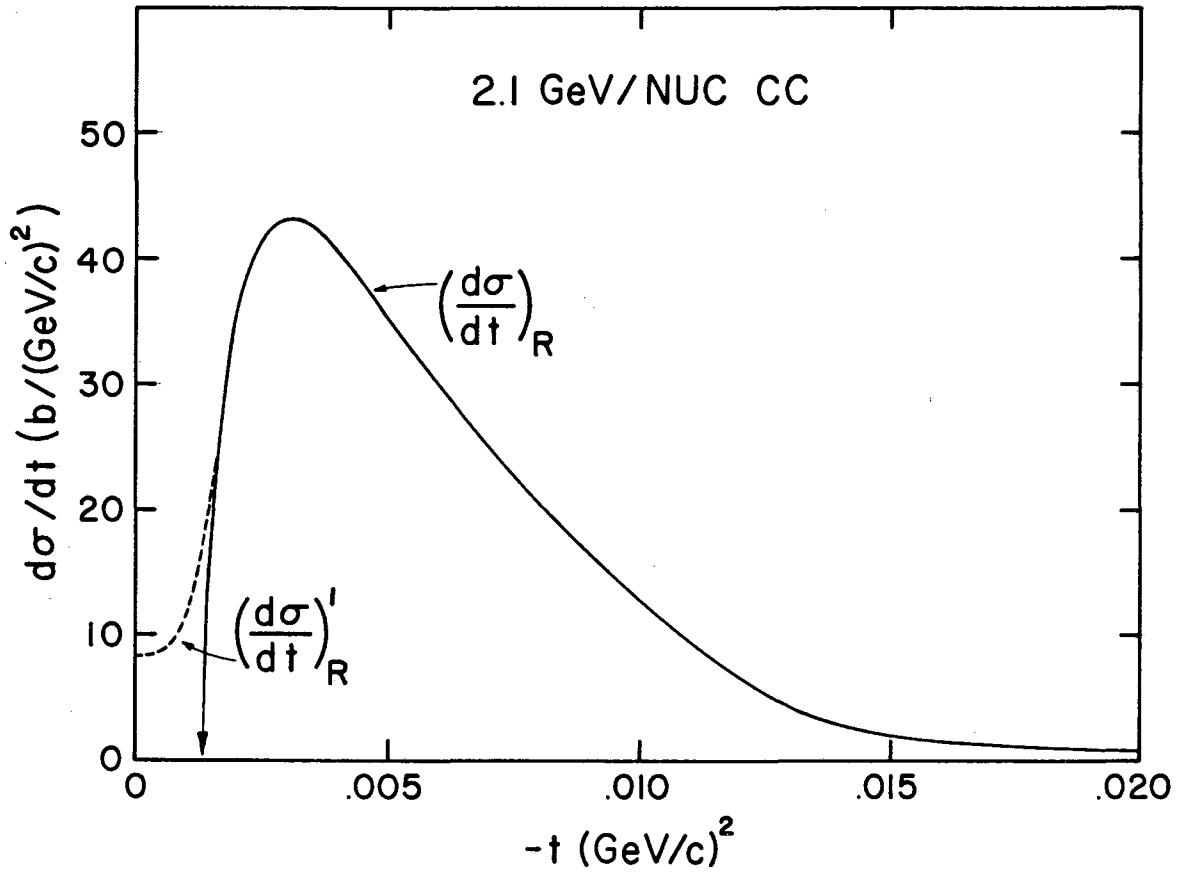
XBL 7511-9051

Fig. 11c

Fig. 12

We divide the "remainder" distribution into two pieces, the straight-throughs and the "remainder" scatters, i.e., the scatters described by $(d\sigma/dt)'_R$. Let $\sigma_R = \int_0^{t_{max}} (d\sigma/dt)'_R dt$. In this approximation the probability that a particle doesn't scatter is $\exp[-\eta(\sigma_{IN} + \sigma_R)]$. Similarly, the probability that a particle interacts according to the scattering law $(d\sigma/dt)'_R$ and doesn't interact inelastically is $[1 - \exp(-\eta\sigma_R)] \exp(-\eta\sigma_{IN})$. The only remaining issue is the angular distribution. Obviously the straight-throughs have $\theta f(\theta) \sim \delta(\theta)$. The remainder scattering can be thought of as a sum of single, double, triple, and so on, scattering terms. The single scattering term has the same angular dependence as the differential cross section, the double is simply the fold of two single scattering distributions, and so on. Since the probability for an interaction is roughly $\eta\sigma_R$, which is typically $\ll 1$, we expect rather small multiple scattering terms. Let us call the weight for the m-scattering term a_m, and denote by $f_m(\theta)$ the distribution of the m-fold scattering, normalized to unity. Then we can give the remainder distribution as

$$\theta f_R(\theta, \ell) = \exp[-\eta(\sigma_R + \sigma_{IN})]\delta(\theta) + [1 - \exp(-\eta\sigma_R)]\exp(-\eta\sigma_{IN})\sum_m a_m f_m(\theta)\theta.$$

Here
$$f_1(\theta) = (d\sigma/dt)'_R$$
$$f_2(\theta) = \frac{1}{2\pi}\int_0^{2\pi} d\phi' \int_0^{\infty} d\theta' \theta' f_1(\theta')f_1(\theta'')$$

and so on.

It is shown in reference (14) (Appendix II) that the weights are given by

$$a_m = (\eta\sigma_R)^m/(m![\exp(\eta\sigma_R) - 1]).$$

In practice we can truncate the series for fairly small values of m (usually 2 or 3), taking care to normalize the sum of the weights to 1.

The folds are all done numerically in a computer program for both target-full and target-empty conditions. We assume that the target-empty scattering, which is actually predominantly from carbon and air, is equivalent to scattering from a small amount of the target-full material. We include the angular distribution of the beam $f_B(\theta)$, which can be obtained from the MWPC data, as further input.

Given the parameters needed to describe the multiple coulomb scattering, the program computes first the Molière distribution and folds it with $f_B(\theta)$, giving $f_M'(\theta)$. The result is renormalized and saved. From the parameters describing the nuclear scattering, $(d\sigma/dt)_R$ is computed where it is well-behaved and smoothly extrapolated to small angles to give $(d\sigma/dt)_R'$. Next we find the various terms $f_m(\theta)$, determine the weights, and combine the distributions to give

$$f_{RT}(\theta) = \sum_{m=1}^{m_{max}} a_m f_m(\theta).$$

Finally we compute

$$f(\theta) = \exp[-\eta(\sigma_R + \sigma_{IN})]f_M'(\theta)$$
$$+ [1 - \exp(-\eta\sigma_R)]\exp(-\eta\sigma_{IN})$$
$$\times \frac{1}{2\pi}\int_0^{2\pi} d\phi' \int_0^\infty \theta' d\theta' f_M'(\theta') f_{RT}(\theta'').$$

Given the angles subtended by the various disk counters, θ_i, we compute

$$D_i = \int_0^{\theta_i} f(\theta)\theta d\theta.$$

Given $f(\theta)$ for both target-full and target-empty conditions, we compute D_i^{full} and D_i^{empty}, then the partial cross section

$$\sigma_i = 1/n \; \ln(D_i^{empty}/D_i^{full}).$$

A chi-squared minimization program then found the optimum values of the nuclear scattering parameters to match the measured partial cross-sections.

The data with proton projectiles were treated slightly differently from the other data. This was done because the elastic scattering could not be separated from the inelastic as cleanly as in the cases of the heavy pro-jectiles.

In the proton-incident cases, the partial cross section was, after subtracting the part that could be attributed to coulomb-nuclear interference, fitted directly to the form

$$\sigma_i \sim \sigma_1 + \sigma_2 e^{bt_i}$$

The total cross section was then taken as the sum of σ_1 and σ_2. Since these fitting parameters are not the true elastic cross section or slope parameter, we do not quote values for these quantities in our results with proton projectiles.

VI. Results

The total cross sections we have measured are shown in Table V. We give both $\sigma_T(A_p A_T)$ and $\sigma_T(A_T A_p)$ in these tables. Since these measurements are obtained with different targets, counter geometries, and correction techniques, their comparison gives a good indication of our probable systematic errors. In general the agreement is excellent and certainly within the errors we consider below. Tables VI and VII give σ_{IN} and b, the elastic scattering slope parameter. These results include the first measurements of σ_T, σ_{IN} and b for nucleus-nucleus interactions for nuclei heavier than deuterons in the 1-GeV/nucleon energy range.

Our results compare favorably to earlier measurements where such a comparison is possible. Besides extensive data on pp and pd reactions, there are measurements on pHe, pC, and dd reported in the literature. $\sigma_T(pp)$ and $\sigma_T(pd)$ agree with the values from Bugg, et al.[13] to within 1.4% and 0.7% respectively. In both cases $\sigma_T(2.1 \text{ GeV/nucleon})$ minus $\sigma_T(0.87 \text{ GeV/nucleon})$ agrees with Bugg et al. to the order of 0.1%. $\sigma_T(pC)$ also agrees with existing data[25] within statistics. Our values of $\sigma_T(pHe)$ are a little lower than those from a previous measurement[25] made at a slightly different energy, but the results are probably consistent within errors. Measurements of $\sigma_T(dd)$ at p = 2.12 GeV/c [compared to our 3.10 and 5.78 GeV/c] have been reported.[26] Since $\sigma_T(pp)$ is varying rapidly in this energy region, direct comparison is risky, but the values agree to ~15%. Our measurements of σ_{IN} for pd, pHe, and pC reactions agree with those reported above to ~10%. Our measurements of b are also consistent with values already reported.[27]

Ableev et al.[28] have recently measured cross sections of alphas on hydrogen, helium, carbon (and other targets) at a beam momentum of 4.5 GeV/c/nucleon. Their values of σ_T, σ_{IN}, and b are very similar to our results.

Table V

TOTAL CROSS SECTION RESULTS

Roman type: statistical error only

Italic type: weighted average of $\sigma_T(A_1A_2)$ and $\sigma_T(A_2A_1)$.
The error quoted is the quadrature of the
statistical error and the systematic error
from Table   X.   If $\sigma_T(A_1A_2)$ differs signi-
ficantly from $\sigma_T(A_2A_1)$, the error is in-
creased to cover the discrepancy.

σ_T(mb)   Target

0.87 GeV/N	p	d	α	C
p	47.94± .1 *47.94± .26*	82.59± .18 *82.5 ± .7*	142.7± .4 *142.7±1.2*	364.7± .8 *364.5± 3.0*
d	81.0 ± .9	151.6 ±1.1 *151.6 ±2.1*	252. ±2.3 *255.5±3.5*	625. ± 5. *617.5± 8.2*
α	143. ±1.6	257.5 ±1.8	390. ±4.2 *390. ±6.3*	820. ±13. *805. ±15.*
C	363 ±2.4	611.5 ±3.5	790. ±7.	1256. ±31. *1256. ±54.*

Target

2.1 GeV/N	p	d	α	C
p	45.54± .1 *45.54± .25*	84.77± .19 *84.65± .7*	147.9± .4 *149. ±1.5*	377.5± .8 *379. ± 3.*
d	83.5 ± .6	158.0 ± .8 *158.0 ±2.1*	262. ±1.8 *267. ±5.*	617.0± 3.0 *630. ±14.*
α	151. ±1.0	271.7 ±1.5	408. ±2.5 *408. ±5.5*	835. ± 5. *830. ±15.*
C	384. ±3.	644. ±3.5	826. ±5.9	1347. ±25. *1347. ±53.*

Projectile

Table VI.

Inelastic Cross-section Results

Roman type: statistical error only.

Italic type: weighted average of $\sigma_{IN}(A_1A_2)$ and $\sigma_{IN}(A_2A_1)$.

The error quoted is the quadrature of the statistical error and the systematic error of 5%. If $\sigma_{IN}(A_1A_2)$ differs significantly from $\sigma_{IN}(A_2A_1)$, the error is increased to cover the discrepancy.

σ_{IN}(mb)	.87 GeV/N		Target		
		p	d	α	C
Projectile	α	120 ±1.7	198 ±2.3	262 ±13	542 ±16
		120 ±6.2	*198 ±10*	*262 ±18.5*	*527 ±26*
	C	262 ±3.3	411 ±3.3	516±5.3	939 ±17
		262 ± 13.5	*411 ±21*	*527 ± 26*	*939 ±49*
	2.1 GeV/N	p	d	α	C
Projectile	d	60±16	134 ±3.3	200.±6.3	431 ±3.5
		60 ±16	*134 ±7.5*	*204.±12*	*426 ±22*
	α	111 ±1.1	205 ±2.8	276 ±3.7	547 ±3
		111 ±5.7	*204 ±12*	*276 ±15*	*535±27*
	C	269 ±2.8	422 ±2.5	523 ±4.6	888 ±19
		269 ±14	*426 ±22*	*535±27*	*888 ±50*

Table VII.

Slope-Parameter Results

Roman type: statistical errors only.

Italic type: weighted average of $b(A_1A_2)$ and $b(A_2A_1)$.

The error quoted is the quadrature of the statistical error and the systematic error of 5%. If $b(A_1A_2)$ is significantly different from $b(A_2A_1)$, the error is increased to cover the discrepancy.

			Target			
$b(GeV/c)^{-2}$	.87 GeV/N		p	d	α	C
Projectile	α		67 ±22 *67 ±22*	61 ±14 *61 ±14*	63 ±10 *63 ±10.5*	120 ±13 *117 ±6.5*
	C		67 ±2.3 *67 ±4*	97 ±1.0 *97 ±5*	117 ±3.0 *117 ±6.5*	254 ±18 *254 ±22*
	2.1 GeV/N		p	d	α	C
Projectile	d		16 ±14 *16 ±14*	61 ±12 *61 ±12.4*	57 ±8.5 *64 ±6*	106 ±4 *100.7±5.2*
	α		31 ±1 *31 ±1.8*	66 ±5 *64 ±6*	70 ±4 *70 ±5*	129 ±4 *123 ±9*
	C		69 ±1.9 *69 ±3.9*	100±1.5 *100.7±5.2*	117 ±2.4 *123 ±9*	204 ±11 *204 ±15*

Our results disagree with the predictions of factorization and agree well with those of Glauber theory. The factorization prediction is that $\sigma_{AA} = (\sigma_{PA})^2/\sigma_{PP}$ where we use the measured values of σ_{PA} and σ_{PP}. In Figure 13 we plot $\sigma_T(AA)$ vs. A and compare our results to the factorization and the Glauber theory predictions. In Table VIII we compare our 2.1 Gev/nucleon results with several theoretical predictions. Except for Tekou[5] the authors have used the optical limit of Glauber theory, which is appropriate for nucleus-nucleus collisions where both nuclei have many nucleons. Overall the agreement between the predictions and our results is quite good. Only $\sigma_T(CC)$ is significantly (more than 10%) below the Glauber theory prediction. A recent calculation in which corrections to the optical limit in the Glauber approximation are made[29] yields a better agreement with our results.

As discussed in Section VII, our insensitivity to excitation and target fragmentation could lead us to underestimate σ_{IN} but not σ_T.

We next turn to a comparison of these cross-sections at different energies. In Figure 14 we plot the quantity $\Delta\sigma/\sigma \equiv [\sigma_T(pA,2.1\ GeV) - \sigma_T(pA,.87\ GeV)]/\sigma_T$ (pA,.87 GeV) vs. A. Although $\sigma_T(pp)$ decreases in this energy range, $\sigma_T(pd)$, $\sigma_T(p\alpha)$ and $\sigma_T(pC)$ all increase. Since deuterons, alphas, and carbon nuclei all have equal numbers of neutrons and protons it is more meaningful to compare to $\frac{1}{2}[\sigma_T(pp) + \sigma_T(pn)]$ instead of $\sigma_T(pp)$ alone. This quantity increases between .87 and 2.1 GeV, but its fractional change is smaller than that for $\sigma_T(pd)$, $\sigma_T(p\alpha)$, or $\sigma_T(pC)$.

The energy dependences of the total cross sections for the other projectiles are plotted vs. the target atomic weight in Figures 15, 16, and 17. The errors
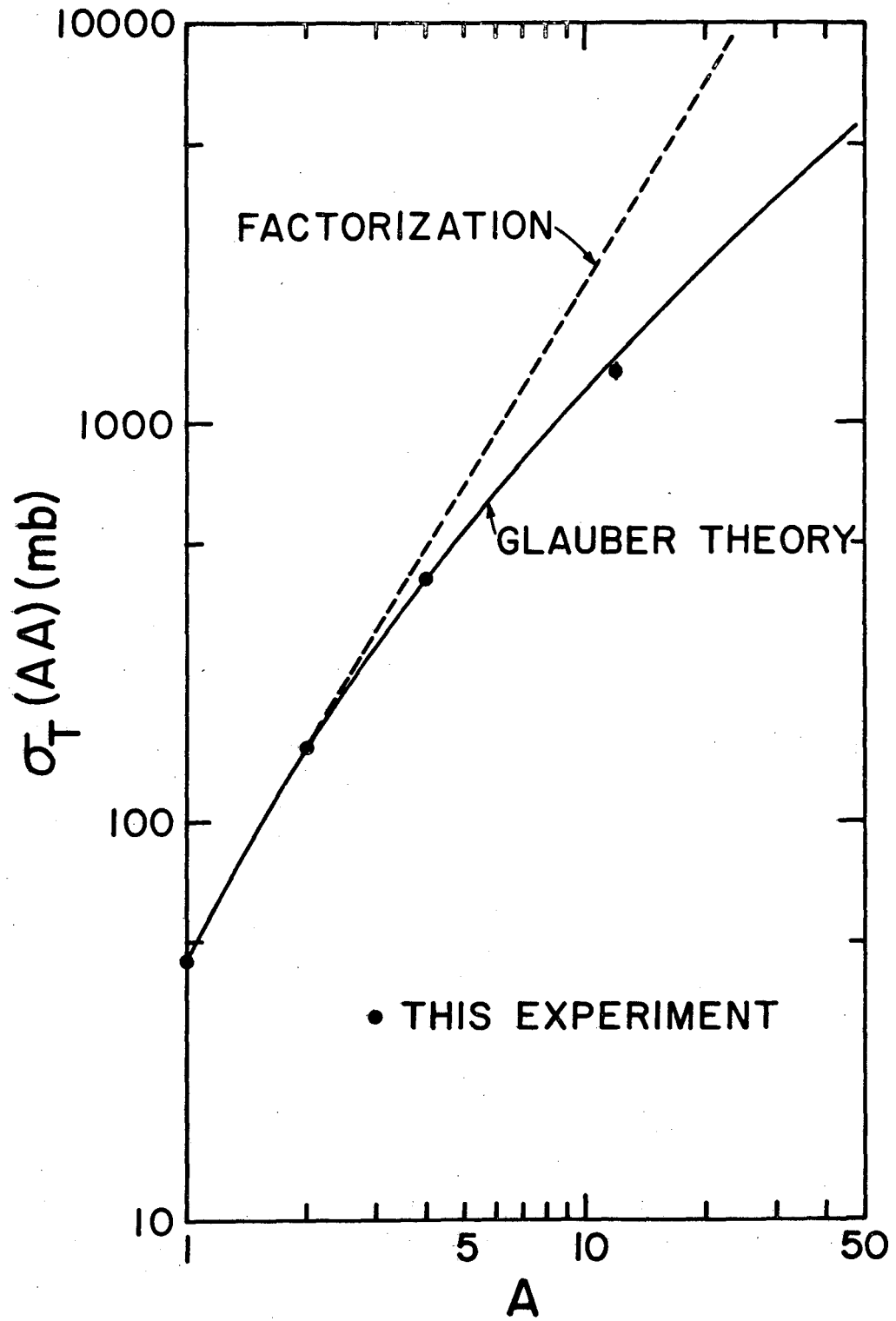
Fig. 13   XBL 7511-9045

Table VIII

Comparison of Experimental Results With
Glauber-theory Predictions

Roman type: results of this experiment at 2.1 GeV/nucleon, taken from Tables V, VI, and VII.

Italic type: predictions of various calculations.

σ_T(mb)	d	α	C
d	158.0±2.1 *154[1]*	267 ±5 *258[1]*	630 ±14 *616[1]*
α		408 ±5.5 *352[2]* *418[3]* *410[4]* *386[5]*	830 ±15 *890[2]* *868[3]* *881[4]* *802[5]*
C			1347±53 *1480[2]* *1600[3,4]* *1420[5]*

(Table VIII continued)

σ_{IN}(mb)	d	α	C
d	134 ±7.5 *124*[1]	204 ±12 *189*[1]	426 ±22 *421*[1]
α		276 ±15 *290*[3]	535 ±27 *560*[3]
C			888 ±50 *950*[3]

b (GeV/c)$^{-2}$	$\alpha\alpha$	αC	CC
	70±5 *67*[3]	123±9 *118*[3]	204±15 *190*[3]

[1]Tekou (reference 5)

[2]Wang (reference 8)

[3]Fishbane and Trefil (reference 7)

[4]Barshay, Dover, and Vary (reference 9)

[5]Franco and Varma (reference 29)
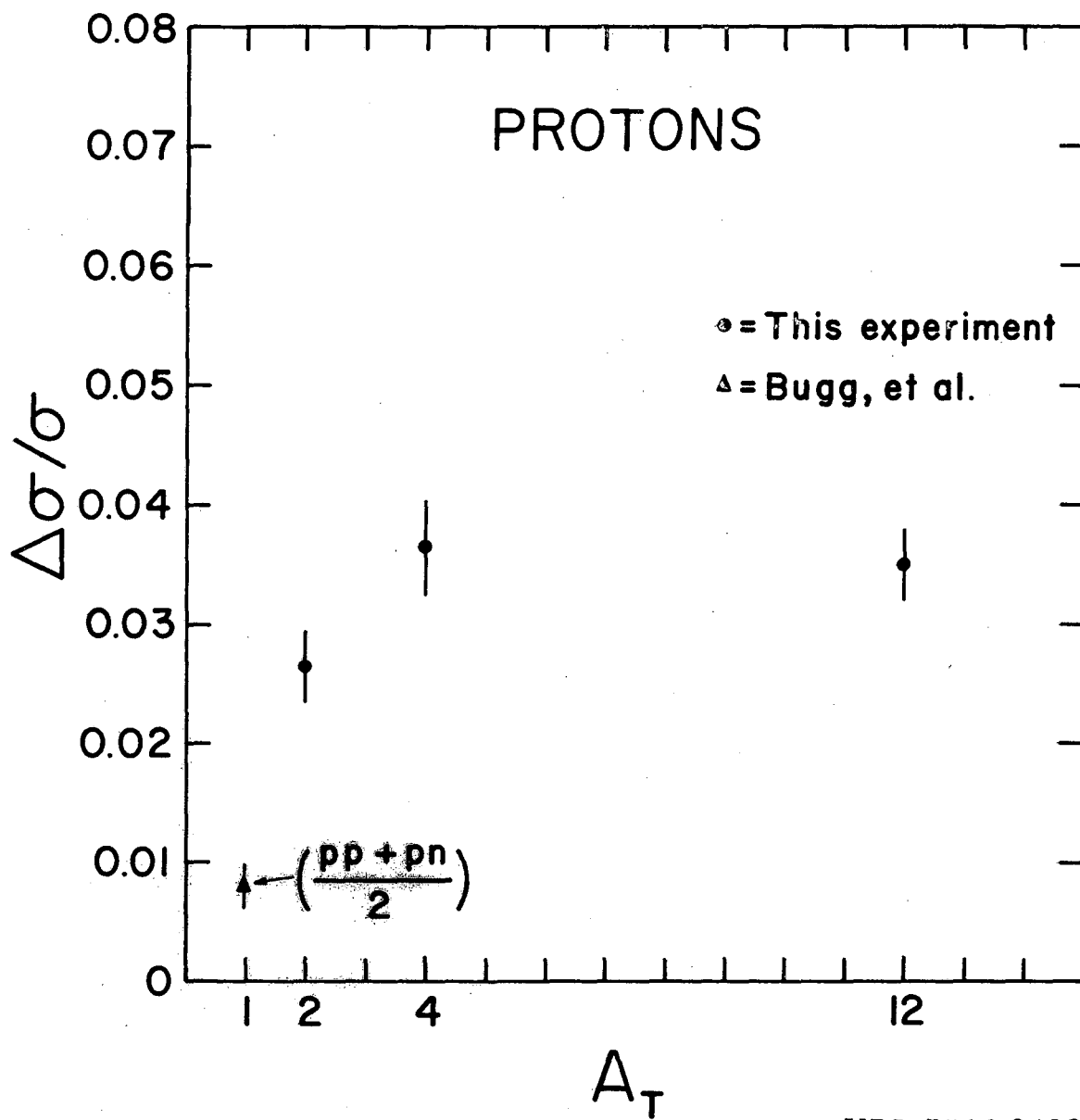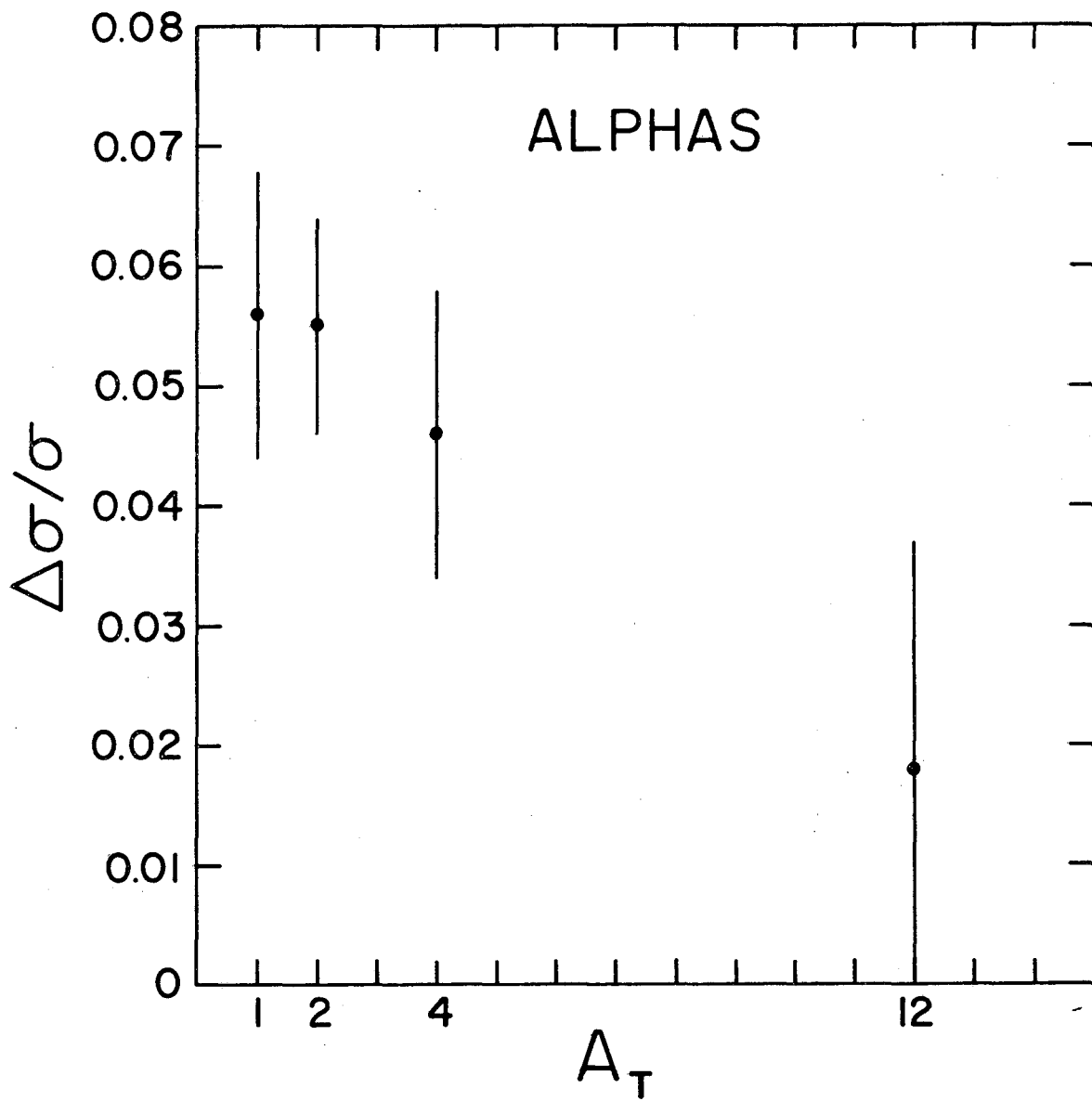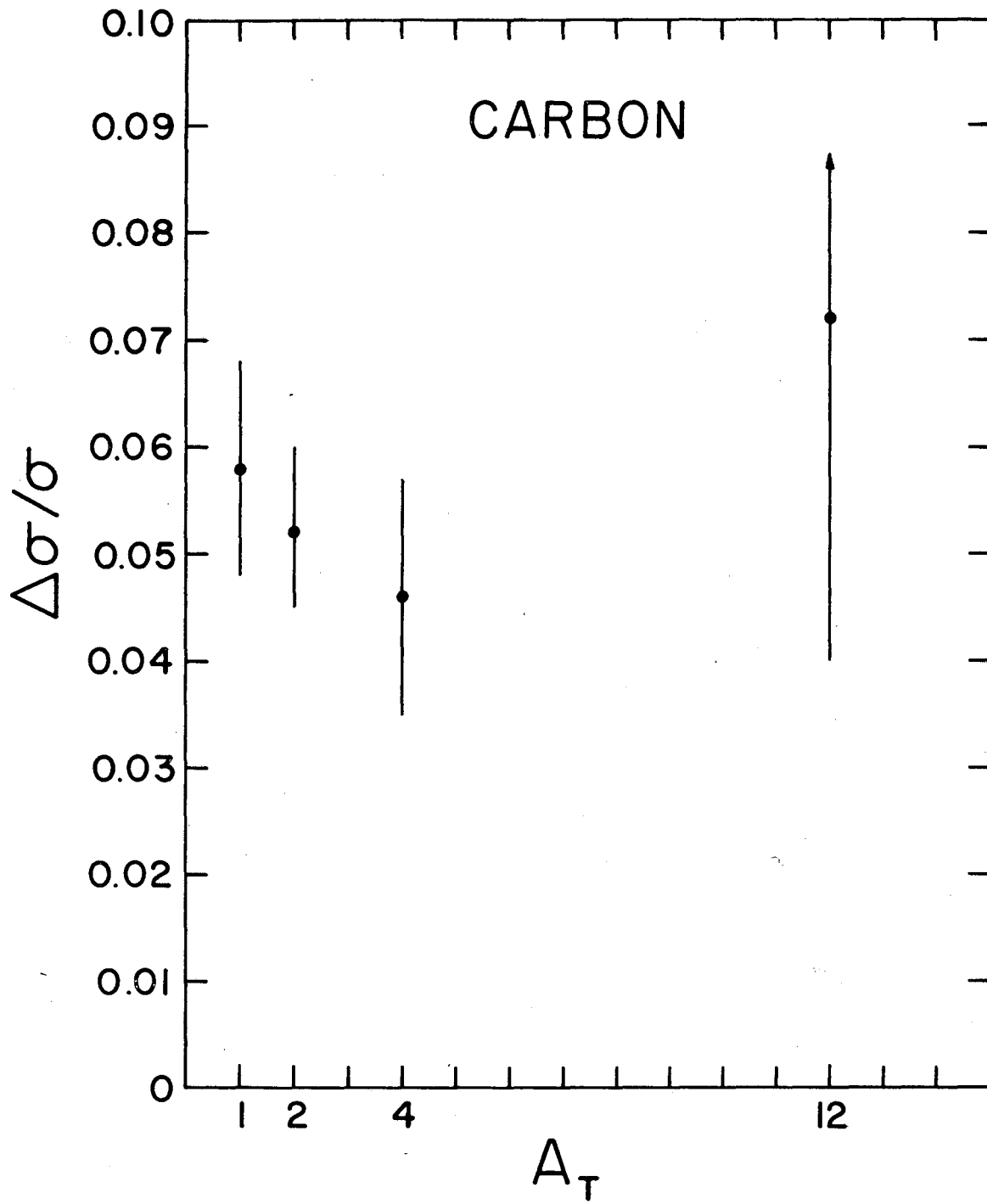
Fig. 14
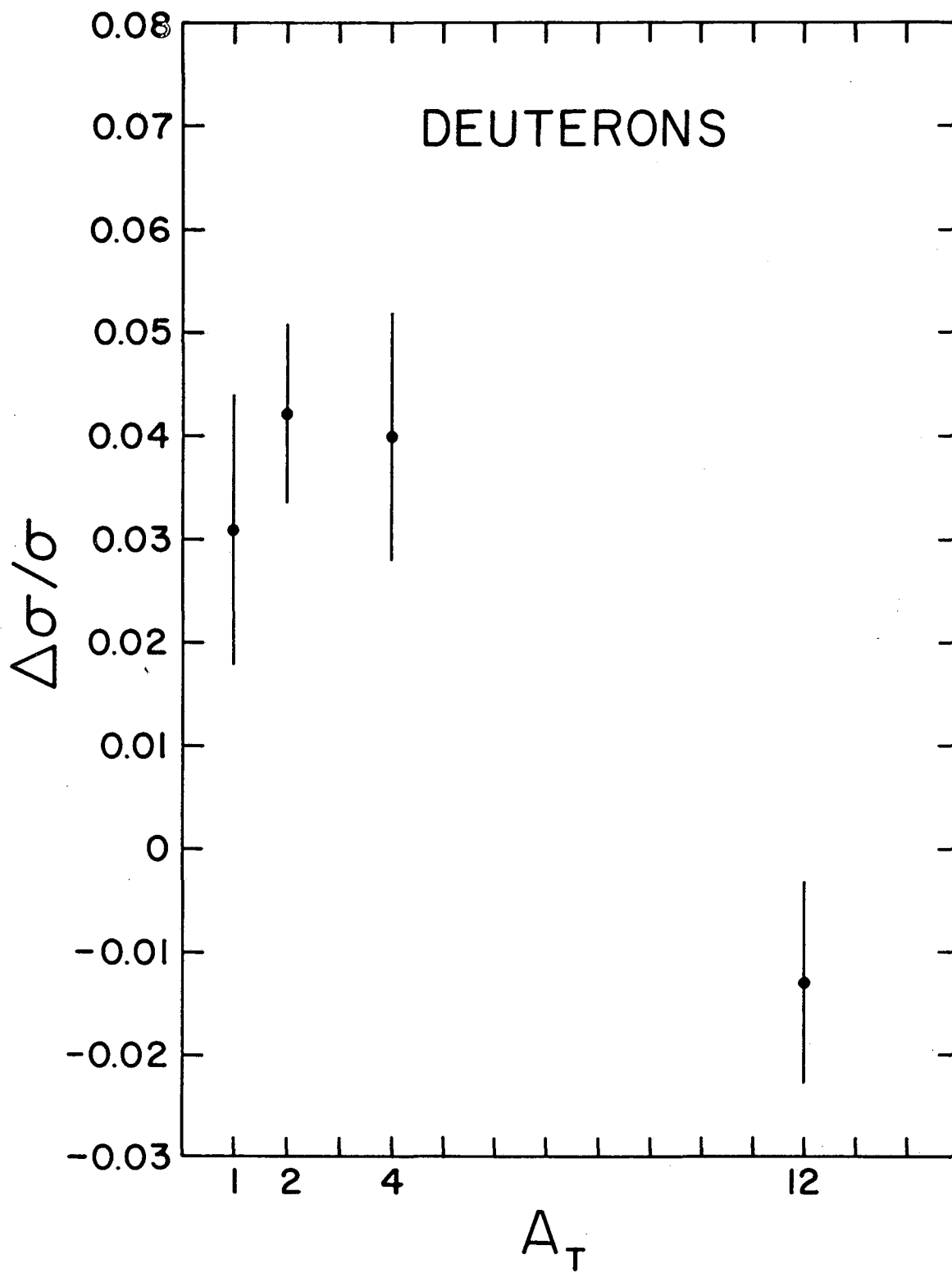
XBL 7510-8493

Fig. 15

XBL 7510-8496

XBL 7510-8494

Fig. 16

XBL 7510-8495

Fig. 17

are statistical only. (Note that the dC and Cd results are inconsistent.) For all the other projectiles, $\Delta\sigma/\sigma$ is generally larger for the heavier targets than for the average of protons and neutrons. It gives some sign of decreasing for $A_T = 12$.

A simple model, such as that of Fishbane and Trefil,[7] predicts that $\Delta\sigma/\sigma$ decreases with increasing size of target and projectile. In such a model the elastic scattering of two nuclei is described as the diffraction of a plane wave by a disk of varying optical density. This density is given by the fold of the matter distributions of the two nuclei. At small radii the disk is essentially black, but it becomes gray at its periphery. As the radii of the interacting nuclei increase, we expect the area of the periphery to become a smaller and smaller fraction of the total area, and hence we expect any energy dependence of the opacity there to become less significant in determining changes in $\sigma_T(A_p A_T)$. We calculate that, for example, if $\sigma_T(NN)$ were to change by 10% between the two energies studied, $\sigma_T(p\alpha)$ should change by 4.5%, $\sigma_T(pC)$ changes by 4%, and $\sigma_T(CC)$ should change by 2%. This model is not quantitatively consistent with the results presented here.

Somewhat better agreement can be obtained by considering the effects of Fermi momentum. Since the nucleons in both the projectile and target are moving (when $A \neq 1$), the energy of any individual nucleon-nucleon collision can vary from the average energy per nucleon of the whole nucleus. From

Figure 18, which shows the energy dependence of $\sigma_T(NN)$, we see that such changes in the energy of a collision at 2.1 GeV/nucleon won't change the cross-section very much. At 0.87 GeV/nucleon, however, the cross-section on the low-energy side changes more than it does on the high-energy side , so $\bar{\sigma}_T(NN) < \sigma_T(NN,.87)$. We have not made detailed calculations to see whether this change in $\sigma_T(NN)$ is sufficient to account for our results, but we note some qualitative success for this picture. Consider $\Delta\sigma/\sigma(pA)$. The deuteron is weakly bound and the Fermi momentum is consequently smaller than that of alphas or carbon nuclei. Thus we expect $\sigma_T(pd,.87)$ to be less affected than $\sigma_T(p\alpha,.87)$. In comparing $\Delta\sigma/\sigma(p\alpha)$ with $\Delta\sigma/\sigma(pC)$, we expect $\bar{\sigma}_T(NN)$ to change by similar amounts for the two cases, since the Fermi momenta are comparable. So we expect $\Delta\sigma/\sigma(p\alpha) = \Delta\sigma/\sigma(pC)$.

Similar arguments apply to the other reactions. When both colliding nucleons have Fermi momentum, we expect $\bar{\sigma}_T(NN)$ to change even more. However, as the nuclei become larger, we expect changes in $\bar{\sigma}_T(NN)$ to become less important.

Several regularities appear in our results which we can understand in simple geometric terms. Figures 19 and 20 show the dependence of the total and inelastic cross-sections on the nucleon numbers of the projectile and target at the two energies studied. We find that the data, excluding the reactions involving protons, are reasonabley well represented by

$$\sigma_T \text{ (in mb)} = 144(A_T^{\frac{1}{3}} + A_P^{\frac{1}{3}} - 1.48)^2$$

$$\sigma_{IN} \text{ (in mb)} = 78(A_T^{\frac{1}{3}} + A_P^{\frac{1}{3}} - 1.25)^2.$$

The obvious picture applies of two nuclei interacting whenever their radii overlap by a certain amount. Note that, as the nuclei involved become large
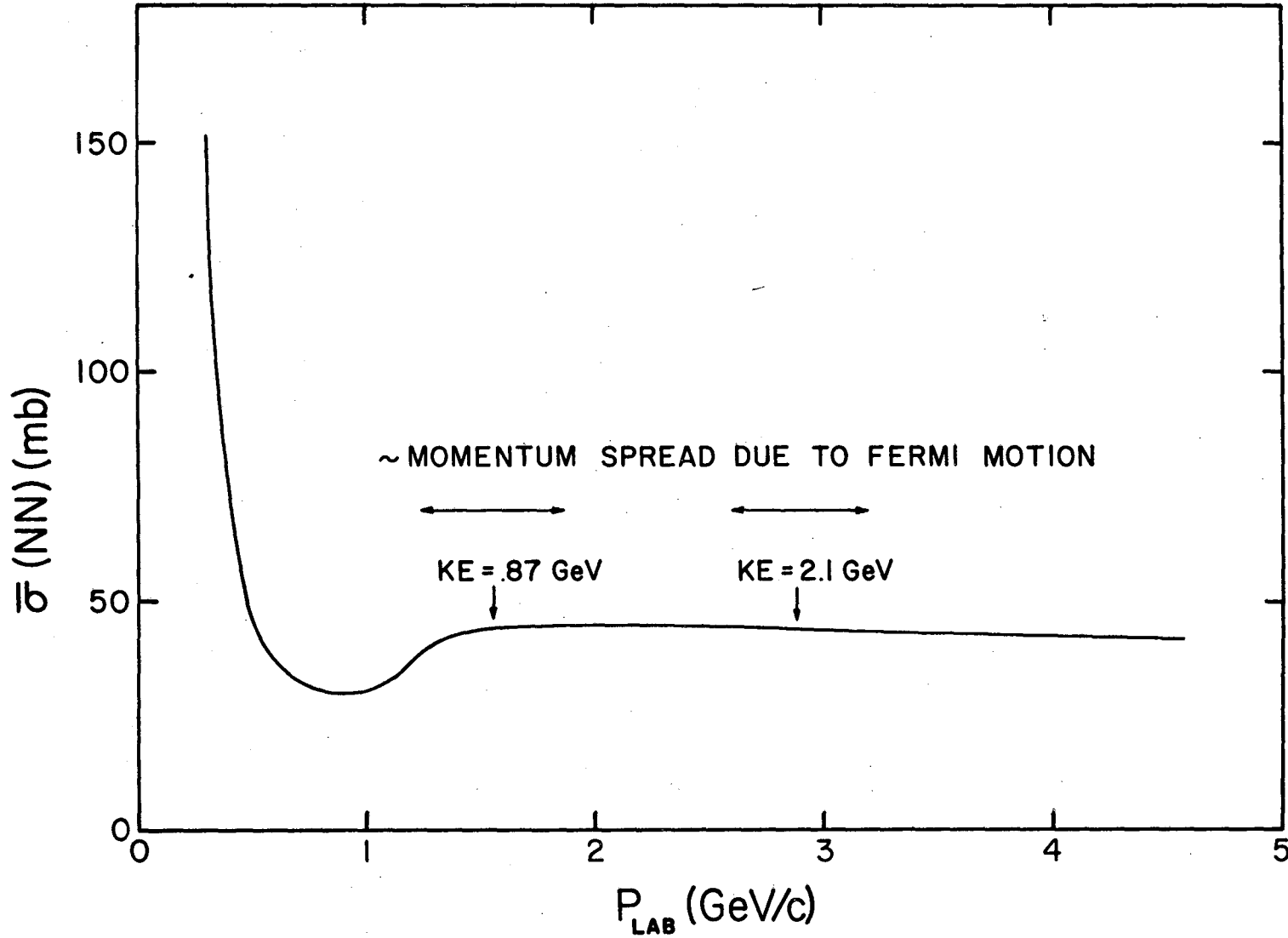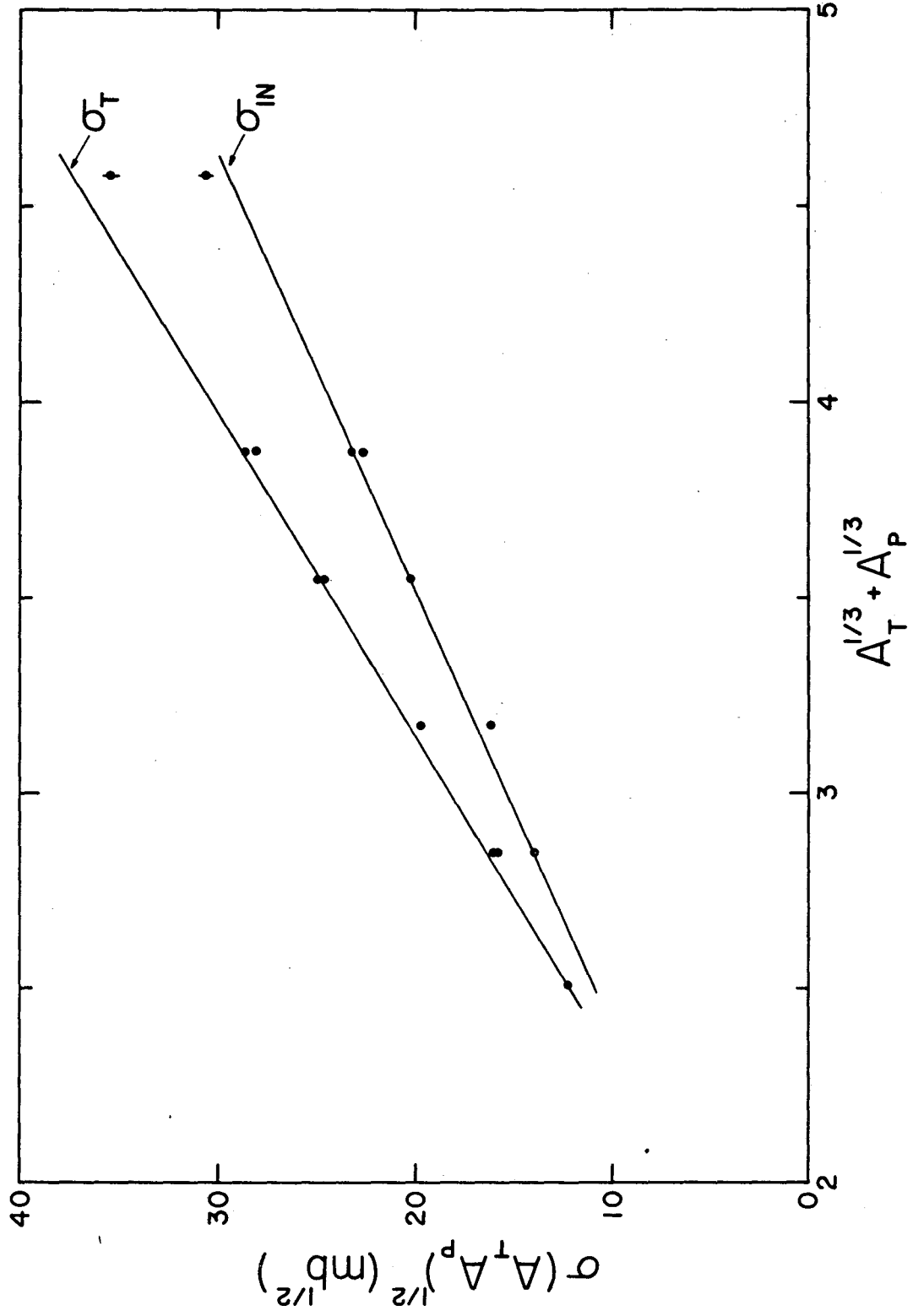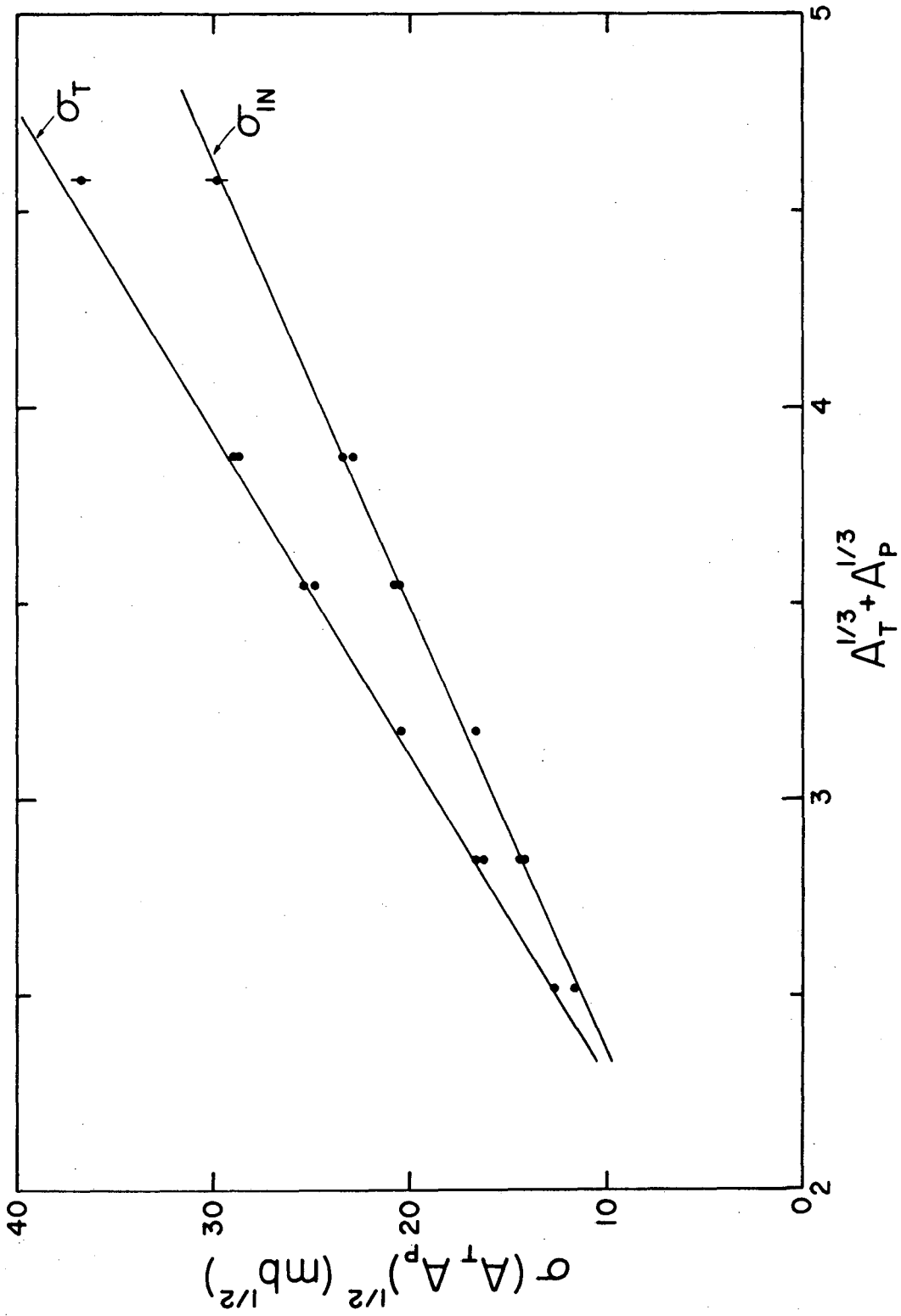
Fig. 18

XBL 7511-9053

$$\sigma_T$$

$$\sigma_{IN}$$

$$A_T^{1/3} + A_P^{1/3}$$

$$\sigma (A_T A_P)^{1/2} \ (mb^{1/2})$$

XBL 7511-9097

Fig. 19

Fig. 20

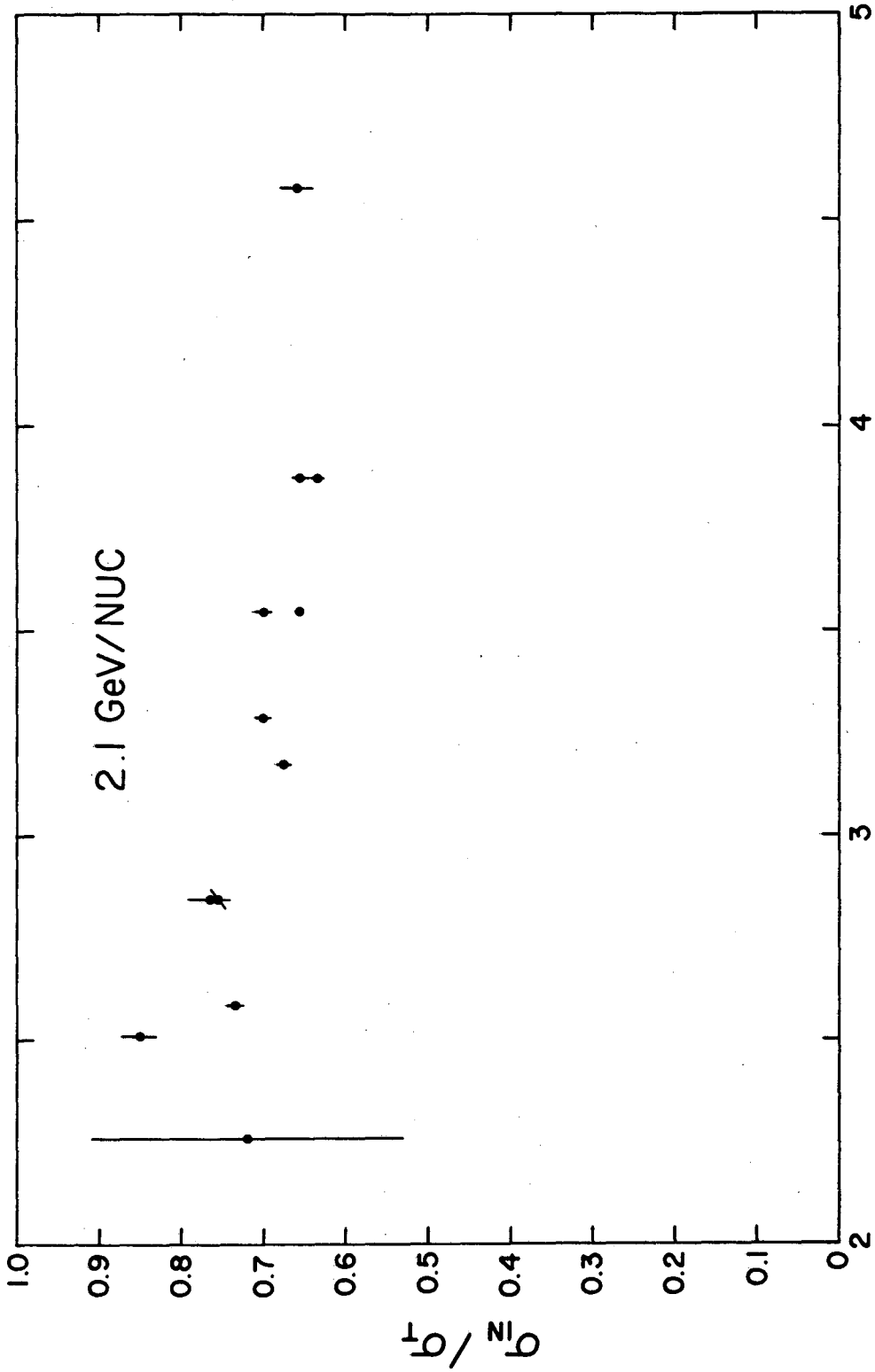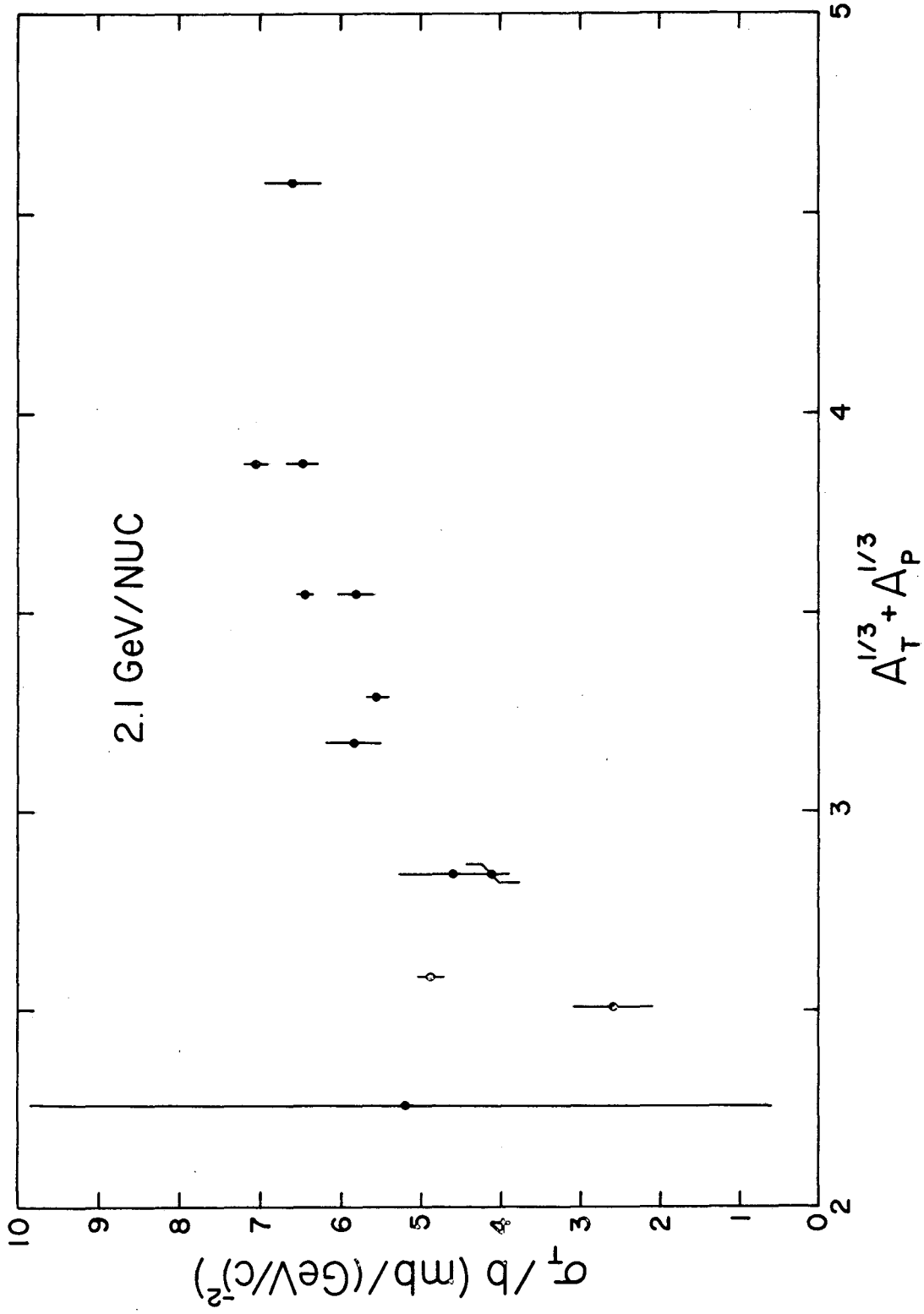XBL 7510-8499

the ratio of inelastic to total cross-section approaches 78/144, close to the limit of 1/2 expected for black disk scattering. In Figure 21 we plot σ_{IN}/σ_T for the 2.1 GeV/nucleon data. Interestingly, in the reactions measured here, this ratio seems to depend only on the overall size of the interaction region, $(A_T^{1/3} + A_P^{1/3})$. We note that σ_{IN}/σ_T decreases as this size increases.

Figure 22 shows σ_T/b vs. $(A_T^{1/3} + A_P^{1/3})$. A black disk has $\sigma_T/b = 8\pi(\hbar)^2$ = 9.8 mb $(GeV/c)^2$. Again the ratio seems to depend primarily on the size of the interaction region.

Fig. 21

XBL 7510-8498

Fig. 22

XBL 7510-8497

VII. Errors

The statistical error in σ_T is due to statistical errors in the partial cross-sections and the uncertainty in extrapolating partial cross sections with finite errors to t = 0. Both our uncertainty in R_i (the normalized number of counts hitting ring i) and in the measured correction factors, g_i (the fraction of the raw events in ring i that correspond to correct-momentum, correct-isotope particles) affect the statistical error associated with σ_i. The errors in the corrected partial cross sections are much larger than the errors in the raw partial cross-section because of statistical uncertainties in the correction factors g_i. The resulting statistical accuracy is about 1% for all the reactions except CC, where it is about 3% (compared to ∿.3% and ∿1%, respectively, for the raw data). Besides the overall statistical uncertainty in σ_T, there is some additional error that arises from the uncertainty in the extrapolation. The σ_i have small errors with respect to each other and so can be fit with some range of parameters σ_T, σ_{IN}, and b. These "fit errors" are usually about one-third the size of the statistical error in the partial cross sections. We add the two in quadrature to estimate the overall error in σ_T and σ_{IN}. The errors in b are the errors associated with the fit alone. The statistical uncertainties in σ_{IN} and b are greater than those in σ_T and in some cases dominate the errors in these quantities.

Many potential sources of experimental error were considered, among them uncertainties in target length, density, position, and contamination; beam contamination; and rate effects. All of these effects are small (typically less than .25%) except for our uncertainty in the hydrogen target density, which was 1%. We estimate our combined experimental uncertainties to be ±0.5%. As discussed in Section IV, we expect errors of order ±1% to result from our

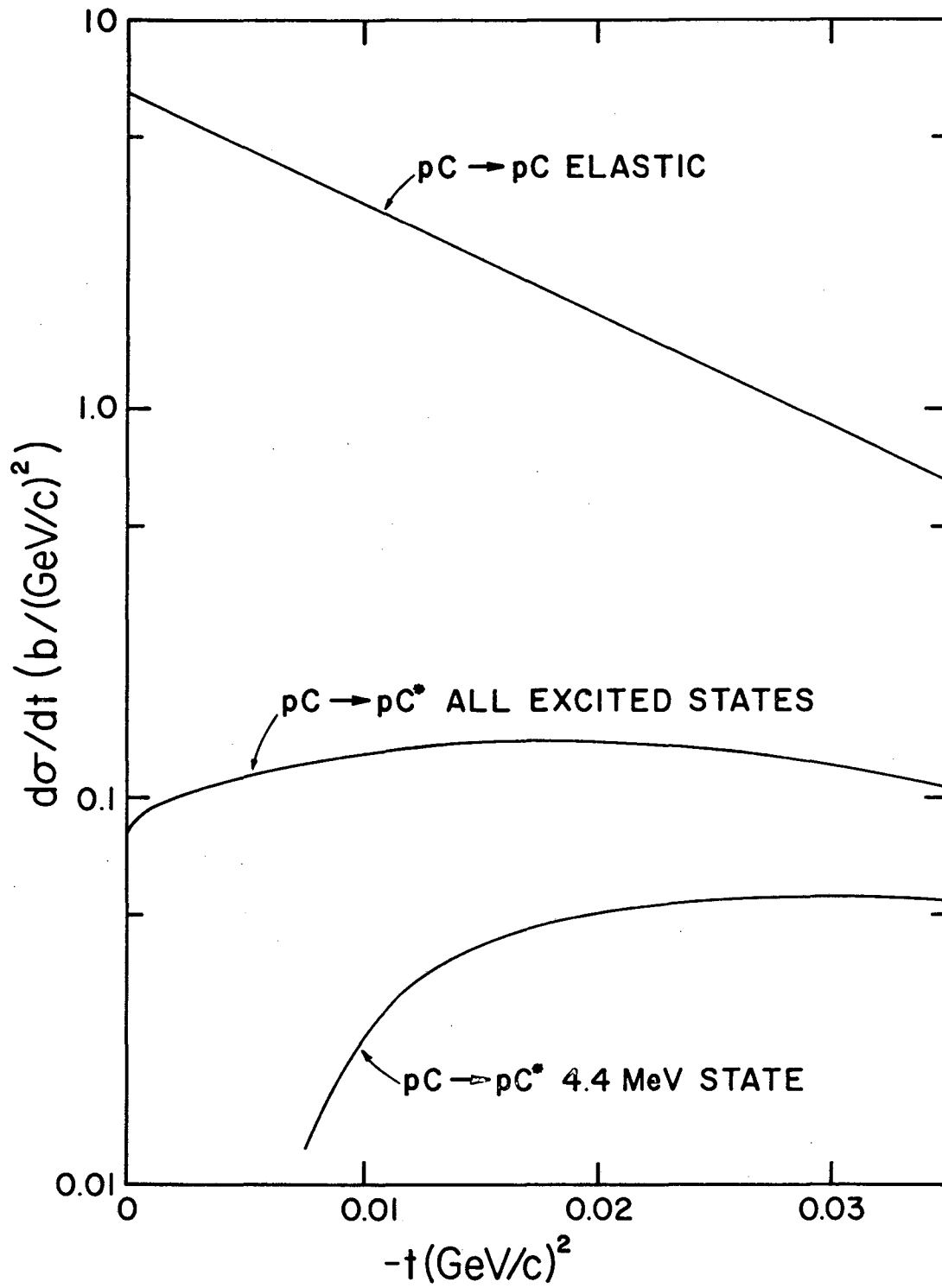uncertainties in making background subtractions and in estimating the correction factors.

The program used to fit the corrected partial cross sections is only accurate to $\pm.5\%$ ($\pm1\%$ for CC reactions). Finally our choices of the ratio, δ, of the real to imaginary parts of the nuclear amplitude and the target-empty length, ℓ_E, are somewhat uncertain. We cannot really estimate our uncertainty in δ, but we do note that changing δ appreciably can change σ_T by one percent or more. Table IX illustrates this fact. Our results depend on the particular values of δ chosen and will be inaccurate if these values are wrong.

Multiple coulomb scattering corrections are crucial only in carbon-initiated reactions. There our uncertainty in ℓ_E (which determines the target-empty coulomb scattering) leads to variations of $\pm3\%$ in $\sigma_T(CC)$ and $\pm1\%$ errors in the other carbon cross sections.

Two other factors must also be considered. First, uncertainties in the data corrections result in uncertainties in σ_{IN} and b of $\pm5\%$. Second, since we lump some inelastic reactions (excitations and target fragmentations which leave the beam intact) with the elastics, we tend to underestimate σ_{IN}. Nuclear excitations and target fragmentations can both give rise to correct-momentum, correct-isotope production and so invalidate our assumption that all such scattering is elastic. In practice, however, neither process contaminates the elastic scattering significantly. We estimated the effect of nuclear excitation (which affects only reactions involving carbon) by referring to some existing measurements[30] made with 156 MeV protons on carbon. Figure 23 shows $d\sigma_x/dt$ for both the excitation of a specific level (4.4 MeV) and the excitation of all levels. The presence of such a background causes us to overestimate σ_E by $\Delta_E = \int_0^{t_{max}} (d\sigma_x/dt)dt$, where $t_{max} = -.030$. Δ_E/σ_E range from 5% (CC) to 10% (pC).

Table IX. Examples of the effect of changing the
Re/Im ratio δ on the total-cross-section
results.

ENERGY/NUCLEON (GeV)	REACTION	δ	σ_T(mb)
.87	pC	.061	359.2
.87	pC	-.1	354.7
.87	CC	.03	1287
.87	CC	-.1	1237

Fig. 23

We underestimate σ_{IN} by the same amount, and so σ_T is unaffected by the presence of excitations.

We expect the errors introduced by target fragmentation to be similar to those just discussed. Again we mistakenly tag some inelastic events as elastic and so overestimate σ_E and understimate σ_{IN}, leaving σ_T unchanged. Since we expect very little target fragmentation without beam fragmentation, and since the average momentum transfers in such collisions are less than .2 GeV/c, we expect very little contamination for $|t| \leq .030$. We expect $\Delta_E/\sigma_E < 5\%$ from target fragmentation. The excellent agreement between $\sigma_T(pC)$, a reaction where the target can fragment, and $\sigma_T(Cp)$, where it cannot, confirms our expectation that the presence of target fragmentation does not affect our measurement of σ_T.

Table X summarizes our estimate of the overall errors in σ_T. We exclude the statistical errors and errors due to wrong choice of δ.

Table X. Estimated systematic errors in σ_T.

TARGET

ERROR IN %	p	d	α	C
p	±.5	±.8	±.8	±.8
d	±1.2	±1.2	±1.2	±1.2
α	±1.2	±1.2	±1.2	±1.2
C	±1.6	±1.6	±1.6	±3.5

PROJECTILE

VIII. Conclusions

The total cross-section results obtained in this experiment are in agreement with the predictions of Glauber-type models and not with simple factorization. They are also in accord with geometrical considerations based on overlapping disks, i.e., $\sigma_T \propto A^{2/3}$.

Experimental complications introduced by Coulomb effects and nuclear fragmentation, and excitation, forced us to introduce several new features such as detailed particle identification and momentum analysis, as well as improved particle trajectory definition, into the traditional transmission-type experiment. The Coulomb effects also made the analysis more complicated than in the case involving the scattering of singly-charged particles. Although the procedure of trying to isolate a "nuclear" cross-section becomes increasingly difficult in the presence of Coulomb effects whose strength is comparable to the nuclear interaction itself, we feel that the folding-type arguments presented in Section V offer a satisfactory solution to this problem for the range of nuclear charges (Z = 1 to 6) studied in this experiment.

IX. Acknowledgements

We thank J. Wiss, D. Nygren, J. Papp, and G. O'Keefe for their help during various phases of this experiment. Our thanks also to S. Olson and K. Lee for their valuable contributions to the data acquisition system.

We wish to express our gratitude to the Bevatron staff, under H. Grunder, for their unflagging efforts to provide us with stable beam conditions and other help. Finally we thank Ms. Jeanne Miller for her efforts in bringing this paper to fruition.

REFERENCES

1. R. J. Glauber, <u>Lectures in Theoretical Physics</u>, Vol. I (Interscience, New York, 1959), p. 315.

2. R. J. Glauber, <u>High Energy Physics and Nuclear Structure</u> (North-Holland, Amsterdam, 1967), p. 311.

3. R. J. Glauber, <u>High Energy Physics and Nuclear Structure</u> (North-Holland, Amsterdam, 1969), p. 207.

4. W. Czyz and L. C. Maximon, Annals of Physics $\underline{52}$, 59 (1969).

5. A Tekou, High Energy Elastic and Quasi-Elastic Deuteron-Nucleus Scattering, International Center for Theoretical Physics preprint No. IC/72/29, Ghana J. Sci. $\underline{14}$, 93 (1974).

6. V. Franco, Phys. Rev. Lett. $\underline{32}$, 911 (1974).

7. P. M. Fishbane and J. S. Trefil, Phys. Rev. $\underline{D10}$, 3128 (1974) and references contained therein.

8. W. L. Wang, Phys. Lett. $\underline{B52}$, 142 (1974).

9. S. Barshay, C. B. Dover, and J. P. Vary, Phys. Lett. $\underline{51B}$, 5 (1974); J. Vary, private communication.

10. V. N. Gribov, Sov. J. Nucl. Phys. $\underline{9}$, 369 (1969).

11. G. Giacomelli, <u>Progress in Nuclear Physics</u>, Vol. 12 (Pergamon Press, New York, 1970), p.77.

12. V. Amaldi, V. T. Cocconi, T. Fazzini, G. Fidecaro, G. Ghesquiere, M. Legros, and H. Steiner, Nuovo Cimento $\underline{46A}$, 171 (1962).

13. D. V. Bugg, D. C. Salter, G. H. Stafford, R. F. George, K. F. Riley, and R. J. Tapper, Phys. Rev. $\underline{146}$, 980 (1966).

14. J. Jaros, Nucleus-Nucleus Total Cross Sections for Light Nuclei at 1.55 and 2.89 GeV/c/nucleon, Thesis, University of California, Berkeley, LBL-3849 (1975).

15. D. E. Greiner, P. J. Lindstrom, H. H. Heckman, B. Cork, F. S. Bieser, Phys. Rev. Lett. 35, 152 (1975).

16. T. Shibata, H. Ejiri, J. Chiba, S. Nagamiya, K. Nakai, H. Bowman, J. Ioannou-Jannou, E. Rauscher, J. O. Rasmussen (to be published).

17. M. Harms, A Multiwire Proportional Chamber Coincidence Matrix, Lawrence Berkeley Laboratory report no. LBL-2053 (unpublished).

18. R. J. Tapper, Tables of Vapour Pressure and Molar Volume for Liquid Hydrogen and Deuterium, Rutherford Laboratory report no. NIRL/R/95 (unpublished).

19. S. Olson, F. Kirsten, E. Binnall, K. Lee, N. Bhandari, and C. C. Nunnally, A Modular Multiwire Readout System for Proportional Wire Chambers, Lawrence Berkeley Laboratory report no. LBL-2354 (unpublished).

20. A. Ashmore in High Energy and Nuclear Physics Data Handbook (Rutherford High Energy Laboratory, Chilton, 1964).

21. H. A. Bethe, Phys. Rev. 89, 1256 (1953).

22. H. A. Bethe, Ann. Phys. (N.Y.) 3, 190 (1958).

23. V. Franco, Phys. Rev. D7, 215 (1973).

24. R. Herman and R. Hofstadter, High Energy Electron Scattering Tables (Stanford University, Stanford, 1960).

25. V. S. Barashenkov, K. K. Gudima, and V. C. Toneev, Forschritte der Physik 17, 683 (1969).

26. A. T. Goshaw, P. J. Oddone, M. J. Baxin, and C. R. Sun, Phys. Rev. Lett. 23, 990 (1969).

27. H. Palevsky, J. L. Friedes, R. J. Sutter, G. W. Bennett, G. J. Igo, W. D. Simpson, G. C. Phillips, D. M. Corley, N. S. Wall, R. L. Stearns, and B. Gottschalk, Phys. Rev. Lett. $\underline{18}$, 1200 (1967).

28. V. G. Ableev, et al., "Experimental Data on Diffraction Elastic Scattering for 17.9 GeV/c α-Particle on Protons and He, C, Al, Cu Nuclei," Joint Institute for Nuclear Research (Dubna) preprint JINR-P1-10565 (1977).

29. V. Franco and G. K. Varma, Phys. Rev. $\underline{C15}$, 1375 (1977). See also references listed therein.

30. D. Hasselgren, P. Roenberg, O. Sunberg, G. Tibbell, Nucl. Phys. $\underline{69}$, 81 (1965).

FIGURE CAPTIONS

Fig. 1. Predictions for $\sigma_T(AA)$ vs. A. The factorization prediction $\sigma_T(AA)$

$= \dfrac{\sigma_T^2(pA)}{\sigma_T(pp)}$ is based on experimentally measured $\sigma_T(pA)$ cross sections.

Fig. 2. Schematic diagram of the attenuation method used in this experiment.

Fig. 3. Partial cross section plot.

Fig. 4. Experimental layout. The beam enters from the left. The disk counters $C_1,...,C_{10}$ are on the movable platform.

Fig. 5. Horizontal beam profiles at the disk counters with and without the matrix in the electronic trigger.

Fig. 6. Trigger and disk counter electronics.

Fig. 7. Pulse-height spectrum for 2.1 GeV/nuc ^{12}C on H_2.

Fig. 8. Bend-angle distribution for 2.1 GeV/nuc ^{12}C on H_2.

Fig. 9. Bend-angle distribution for 0.87 GeV/nuc α on He. (a) All events. (b) Ring-7 events.

Fig. 10. Pulse-height spectrum for .87 α on He.

Fig. 11. (a) Model calculation of $d\sigma/dt(pp)$ vs. t.

(b) Model calculation of $d\sigma/dt(pC)$ vs. t.

(c) Model calculation of $d\sigma/dt(CC)$ vs. t.

Fig. 12. $(d\sigma/dt)_R$ vs. -t.

Fig. 13. Predictions and results for $\sigma_T(AA)$ vs. A.

Fig. 14. $\Delta\sigma/\sigma$ vs. A_T for protons incident, with statistical errors only.

Fig. 15. $\Delta\sigma/\sigma$ vs. A_T for deuterons incident, with statistical errors only.

Fig. 16. $\Delta\sigma/\sigma$ vs. A_T for alphas incident, with statistical errors only.

Fig. 17 $\Delta\sigma/\sigma$ vs. A_T for carbon incident, with statistical errors only.

Fig. 18. $\bar{\sigma}(NN)$ vs. P_{lab}.

Fig. 19 $\sigma(A_p A_T)^{1/2}$ vs. $(A_T^{1/3} + A_p^{1/3})$ at .87 GeV/nucleon.